The Astrophysical Journal, 956:91 (17pp), 2023 October 20 https://doi.org/10.3847/1538-4357/acf314

Unraveling the Complexity of Dwarf Galaxy Dynamics: A Study of Binary Orbital Motions

Wenting Wang[1,2], Ling Zhu[3], Yipeng Jing[1,2], Robert J. J. Grand[4,5,6], Zhaozhou Li[1,2,7], Xiaoting Fu[8], Lu Li[3], Jiaxin Han[1,2], Ting S. Li[9,10], Fabo Feng[11,12], and Carlos Frenk[13]

[1] Department of Astronomy, Shanghai Jiao Tong University, Shanghai 200240, People's Republic of China; wenting.wang@sjtu.edu.cn
[2] Shanghai Key Laboratory for Particle Physics and Cosmology, Shanghai 200240, People's Republic of China
[3] Shanghai Astronomical Observatory, Chinese Academy of Sciences, 80 Nandan Road, Shanghai 200030, People's Republic of China
[4] Astrophysics Research Institute, Liverpool John Moores University, 146 Brownlow Hill, Liverpool, L3 5RF, UK
[5] Instituto de Astrofísica de Canarias, Calle Vía Láctea s/n, E-38205 La Laguna, Tenerife, Spain
[6] Departamento de Astrofísica, Universidad de La Laguna, Av. del Astrofísico Francisco Sánchez s/n, E-38206, La aguna, Tenerife, Spain
[7] Centre for Astrophysics and Planetary Science, Racah Institute of Physics, The Hebrew University, Jerusalem 91904, Israel
[8] Purple Mountain Observatory, Chinese Academy of Sciences, 10 Yuanhua Road, Nanjing 210023, People's Republic of China
[9] David A. Dunlap Department of Astronomy & Astrophysics, University of Toronto, 50 St. George Street, Toronto, ON, M5S3H4 Canada
[10] Dunlap Institute for Astronomy & Astrophysics, University of Toronto, 50 St George Street, Toronto, ON M5S 3H4, Canada
[11] Tsung-Dao Lee Institute, Shanghai Jiao Tong University, Shengrong Road 520, Shanghai, 201210, People's Republic of China
[12] School of Physics and Astronomy, Shanghai Jiao Tong University, 800 Dongchuan Road, Shanghai 200240, People's Republic of China
[13] Institute for Computational Cosmology, Department of Physics, Durham University, South Road, Durham DH1 3LE, UK
Received 2023 June 7; revised 2023 August 16; accepted 2023 August 21; published 2023 October 11

Abstract

We investigate the impact of binary orbital motions on the dynamical modeling of dwarf galaxies with intrinsic line-of-sight velocity dispersions (σ_{v_r}) of 1–9 km s^{-1}. Using dwarf galaxies from the AURIGA level-2 and level-3 simulations, we apply the Jeans Anisotropic Multi-Gaussian Expansion modeling to tracer stars before and after including binaries to recover the dynamical masses. The recovered total masses within the half-mass radius of tracers, $M(< r_{\rm half})$, are always inflated due to binary motions, with greater inflations occurring for smaller σ_{v_r}. However, many dwarf galaxies experience central density *deflated* due to binary motions, with little dependence on σ_{v_r}. This is due to the negative radial gradients in the velocity dispersion profiles, with the fractional inflation in σ_{v_r} due to binaries more significant in outskirts. An extreme binary fraction of 70% can lead to central density deflation of up to 10%–20% at 3 km s^{-1} $< \sigma_{v_r} <$ 8 km s^{-1}, with $M(< r_{\rm half})$ inflated by 4% at 9 km s^{-1} and up to 15% at 3 km s^{-1}. A lower binary fraction of 36% leads to similar deflations, with the inflations decreasing to approximately 10% at 3 km s^{-1} and becoming statistically insignificant. The choice of binary orbit distribution models does not result in significant differences, and observational errors tend to slightly weaken the deflations in the recovered central density. Two observations separated by 1 yr to exclude binaries lead to almost zero inflations/deflations for a binary fraction of 36% over 3 km s^{-1} $< \sigma_{v_r} <$ 9 km s^{-1}. For $\sigma_{v_r} \sim$ 1 km s^{-1} to 3 km s^{-1}, a binary fraction of 70% (36%) still results in 60% (30%) to 10% (1%) of inflations in $M(< r_{\rm half})$, even with two-epoch observation.

Unified Astronomy Thesaurus concepts: Dwarf galaxies (416); Hydrodynamical simulations (767); Dark matter (353); Binary stars (154)

1. Introduction

Understanding the dark matter content and inner density profiles of dwarf galaxies has long been a hotly debated topic in galaxy formation and cosmology. For example, the so-called "core-cusp" problem has been raised to the standard theory, in the way that dark-matter-only simulations predict inner density slopes close to −1 (cusp), whereas the modeling of gas rotation curves or stellar kinematics in the central regions of low surface brightness galaxies, gas-rich dwarfs, and dwarf spheroids favors inner slopes close to 0 (core), which is in tension with the theory (e.g., Flores & Primack 1994; Moore 1994; de Blok et al. 2001; Gentile et al. 2004; de Blok 2010; Bullock & Boylan-Kolchin 2017). Additionally, the discoveries of dwarf galaxies with very low fractions or no dark matter has invoked puzzles to the theory as well, because dwarf galaxies are believed to be typically dark-matter-dominated systems (e.g., McConnachie et al. 2008; Martin et al. 2009; Torrealba et al. 2016, 2019; Collins et al. 2020, 2021).

Observationally, constraints on the dark matter content of dwarf galaxies are usually based on dynamical modeling of observed member stars or gas rotation curves, while it has been pointed out that invalid assumptions behind various types of dynamical models may cause wrong conclusions, especially for individual or small sample systems (e.g., Genina et al. 2018; Wang et al. 2022). In addition to the classical Milky Way (MW) dwarfs, a large number of dwarf spheroidal satellite galaxies have been discovered around our MW. These objects are much fainter, having larger mass-to-light ratios and velocity dispersions in the range of $<\sim$3 km s^{-1} to 7–8 km s^{-1}. Modeling of these fainter dwarf galaxies is even more susceptible to errors than more massive MW classical dwarf galaxies.

The sources of errors not only include statistical ones, because such faint dwarf galaxies usually have a small number of member stars observed, but also, more importantly, include

systematic errors such as the contamination by foreground stars and inflation of the velocity dispersion due to orbital motions of binary stars. The binary orbital motion is the most difficult to be corrected, which not only depends on a correct estimate of binary fraction in the tracer star sample based on multiepoch observations of the line-of-sight velocities (LOSVs), but also requires a good knowledge of the binary orbital element distributions.

With orbital element distributions constrained from solar neighborhood stars, dwarf spheroids with velocity dispersions of 4–10 $\mathrm{km\,s^{-1}}$ are claimed unlikely to have their intrinsic dispersions significantly inflated by more than 20%–30% (e.g., Hargreaves et al. 1996; Minor et al. 2010). On the other hand, since the typical velocities of binary orbital motions can reach a few kilometers per second, dwarf systems with intrinsic dispersions $<\sim 4\,\mathrm{km\,s^{-1}}$ have a greater risk of having their velocity dispersions more significantly boosted (e.g., Martin et al. 2007; Simon & Geha 2007; McConnachie & Côté 2010; Koposov et al. 2011; Spencer et al. 2017; Minor et al. 2019; Pianta et al. 2022). Note that, in some previous studies, 3σ clippings of extreme velocities are applied, and sometimes multiepoch data are used to exclude binaries.

Most of the previous analysis, however, was based on Monte Carlo simulations with Gaussian intrinsic velocity dispersions. Real dwarf galaxies can have negative radial gradients in their velocity dispersion profiles, with higher dispersions in the very center, and lower dispersions in outskirts. For example, prominent negative radial gradients were seen in a few classical dwarf spheroids, such as in the metal-rich population of Sculpter (e.g., Battaglia et al. 2008; Zhu et al. 2016a), and in the metal-poor populations of Ursa Minor (e.g., Pace et al. 2020) and of Fornax (e.g., Amorisco & Evans 2012). For ultra-faint dwarfs,[14] the velocity dispersions of which are usually believed to be most significantly affected by binaries, their number of observed stars is currently too few to enable robust measurements of radial gradients. However, if the velocity dispersion profiles are radius dependent, the total mass enclosed within different radii would be biased by binary orbital motions to different levels. Thus, investigating more realistically simulated dwarf galaxy systems could bring new insights toward how binary orbital motions affect the constraints on the underlying density profiles of dwarf galaxies.

The resolution limit of ultra-faint dwarf galaxies in modern simulations is a crucial issue. Individual stars are not resolved yet, and the star particles in present-day hydrodynamical simulations represent single stellar populations. The average stellar masses of star particles or gas cells are often on the order of $>\sim 10^{4-5}\,M_\odot$. For example, the baryonic particle mass of the IllustrisTNG50 simulation is $\sim 10^4\,M_\odot$ (Pillepich et al. 2019). For dwarf galaxies with stellar masses of $10^{4-5}\,M_\odot$, their velocity dispersions usually range from a few to 10 $\mathrm{km\,s^{-1}}$. Though their velocity dispersions are likely inflated by binaries (e.g., Hargreaves et al. 1996; Minor et al. 2010), the number of tracer star particles is too few for proper dynamical modelings. There are only a few to about ten star particles for $10^{4-5}\,M_\odot$ dwarfs in TNG50.

The resolution is significantly higher in the cosmological zoomed-in hydrodynamical simulation, AURIGA (Grand et al. 2017), which is particularly aimed at resolving the evolution of MW-mass systems and their population of satellites. For example, the level-2 suite of AURIGA simulations has an average star particle mass of $\sim 800\,M_\odot$. Hence, for dwarfs with stellar masses of $10^{4-5}\,M_\odot$, they can have a few tens up to a few thousands of star particles, enabling the investigations on how binary orbital motions affect the mass constraints for more realistic dwarf systems in modern hydrodynamical simulations.

In this paper, we take advantage of the AURIGA simulations. Since binaries are not resolved, we incorporate binary orbital motions by sampling their orbital element distributions based on different models, while the original motions of star particles are treated as the motions of barycenters for binaries. We start with the so far highest resolution of level-2 simulations. Moreover, since level-2 has only one MW-like system so far and with a few tens of star particles as tracers at the low-mass end, the statistical errors are still large, we will also use the lower-resolution suite of level-3 simulations plus a scaling method. The AURIGA simulations and the scaling approach have enabled us to investigate the effect of binaries upon constraining the underlying density profiles, and in particular, our analysis is based on more realistic dwarf systems with radius-dependent velocity dispersion profiles. The best-constrained mass at different radii can be directly compared before and after incorporating binary motions. Note, however, we do not evaluate the performance of JAM in this paper, since the focus of this paper is the effect of binary motions. We refer the readers to Wang et al. (2022; hereafter Paper I) about the performance of JAM, in which we have performed detailed investigations on how the best fits by JAM may deviate from reality for dwarf systems in AURIGA simulations.

The layout of the paper is as follows. We first introduce the AURIGA suite of simulations, sample of simulated dwarf galaxy systems, mock stars and the models of binary orbital element distributions in Section 2. Our dynamical modeling approach is the axisymmetric Jean Anisotropic multi-Gaussian expansion method (Section 3). The model constraints and the comparison before and after including binaries will be shown in Section 4, with discussions on different binary models and binary fractions, with or without observational errors and multiepoch observations. We discuss and conclude in the end (Section 5).

2. Data

In this section, we first introduce the AURIGA simulations. We then move on to introduce the selection of dwarf galaxies, mock stars, the incorporation of binary motions, the creation of mock galaxy images and multi-Gaussian decomposition of the stellar component.

2.1. The AURIGA Suite of Simulations

Details about the AURIGA simulations can be found in Grand et al. (2017) and Grand et al. (2018). Here we make a brief introduction.

The AURIGA simulations are a suite of cosmological zoomed-in simulations, with the parent systems identified as those isolated and MW-mass halos from the dark-matter-only simulations of the EAGLE project (Schaye et al. 2015), the evolution of which are re-simulated with higher resolutions and traced from redshift $z = 127$ to $z = 0$. The cosmological parameters adopted are from the third-year Planck data (Planck Collaboration et al. 2014) with $\Omega_m = 0.307$, $\Omega_\Lambda = 0.693$, $\Omega_b = 0.048$, and $H_0 = 67.77\,\mathrm{km\,s^{-1}\,Mpc^{-1}}$.

[14] Ultra-faint dwarf galaxies are typically defined to have stellar masses smaller than $10^5\,M_\odot$ (e.g., Simon 2019; Orkney et al. 2021).

The simulations were performed using the magnetohydrodynamical code AREPO (Springel 2010) with full baryonic physics, which incorporates a comprehensive galaxy formation model. The physical mechanisms of the galaxy formation model include atomic and metal line cooling (Vogelsberger et al. 2013), a uniform UV background (Faucher-Giguère et al. 2009), a subgrid model of the interstellar medium and star formation processes (Springel & Hernquist 2003), metal enrichment from supernovae and AGB stars (Vogelsberger et al. 2013), feedback from core collapse supernovae (Okamoto et al. 2010), and the growth and feedback from supermassive black holes (Springel et al. 2005). A uniform magnetic field with comoving strength of 10^{-14} G is set at redshift $z = 127$, which quickly becomes subdominant in collapses halos (Pakmor & Springel 2013; Pakmor et al. 2017).

We will use the "level-2" and "level-3" resolutions of AURIGA simulations. There are six MW-like systems in the level-3 simulations, named Au6, Au16, Au21, Au23, Au24, and Au27. The virial masses[15] of their host dark matter halos are in the range of 1–2 $\times 10^{12}\,M_{\odot}$, to represent the virial mass of our MW (e.g., Wang et al. 2020, 2015). The typical dark matter particle mass of level-3 resolution is about $4 \times 10^{4}\,M_{\odot}$, while the average baryonic particle mass is about $5 \times 10^{3}\,M_{\odot}$. More recently, Au6 has been re-simulated with level-2 resolution. It has a baryonic mass resolution of $\sim$800 $M_{\odot}$. There are approximately 5 times as many satellite galaxies at this high resolution compared to a standard baryonic resolution simulation of $10^{4-5}\,M_{\odot}$ for the same system (Grand et al. 2021). Note level-3 and level-2 resolutions will meet different purposes in this study, which will be explained in Section 2.2.

2.2. Dwarf Galaxies

Each of the MW-like systems in level-3 and level-2 simulations has its dwarf satellite galaxies. For dwarfs with stellar masses of $10^{4-5}\,M_{\odot}$, the number of available star particles ranges from only $<\sim$10 to at most a few hundred in level-3, while the level-2 resolution can have a few tens to $>\sim$1000 star particles as tracers.

We first use the population of dwarf galaxies in the level-2 simulation for initial analysis. We select dwarf systems that are less massive than $10^{7.5}\,M_{\odot}$ in stellar mass and also have more than 40 star particles. Massive dwarfs with stellar masses much greater than $10^{5}\,M_{\odot}$ are unlikely to be significantly affected by binary orbital motions upon dynamical modeling, but we include them for comparisons with less-massive systems. In addition, systems with minor axes strongly misaligned with their spin axes severely deviate from axisymmetry and cannot be well fit by our dynamical modeling method, which are excluded from our analysis. In the end, we have 17 dwarf systems from level-2 (see Section 3 for details).

On the other hand, although the lower limit of 40 star particles corresponds to approximately $\sim 3 \times 10^{4}\,M_{\odot}$ in level-2 and 40 tracers enables reasonable dynamical constraints, the statistical errors in the best fits are quite large. Additionally, with only a few tens of star particles, the internal dynamics of dwarf systems might not be well resolved, hence, preventing us from robust investigations on systematics introduced by binaries based on level-2 resolution. We thus only use level-2 for initial analysis, and will focus on discussing results based on level-3 simulations with a scaling method.

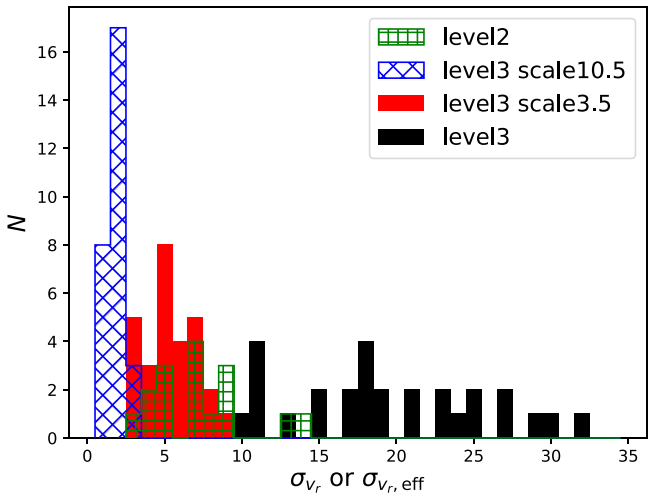

Figure 1. Black, red, and blue histograms are the line-of-sight velocity (LOSV) dispersions of dwarf galaxies selected from the AURIGA level-3 simulations. The black histogram shows the original LOSV dispersions, on the basis of which the velocity dispersions of the red and blue histograms are manually reduced by factors of 3.5 and 10.5, respectively. The original stellar masses of these level-2 systems are in the range of $10^{7.5}$–$10^{9}\,M_{\odot}$. The scaling has enabled us to equivalently treat them as lower-mass dwarf galaxies when investigating the effect of binary motions, while still maintaining a requisite number of star particles as tracers. The green histogram is based on dwarf galaxies from the AURIGA level-2 simulations with stellar masses smaller than $10^{7.5}\,M_{\odot}$.

We select dwarf galaxies having at least 6000 star particles from the level-3 simulations. This corresponds to a lower limit of $\sim 10^{7.5}\,M_{\odot}$ in stellar mass. The large number of star particles to be used as dynamical tracers can suppress the size of statistical errors, but massive dwarfs with stellar masses greater than $10^{7.5}\,M_{\odot}$ are unlikely to have their velocity dispersions significantly boosted by binary orbital motions. Hence, we will manually increase the LOSVs due to binary orbital motions (see Section 2.4 and Equation (1)) by factors of 3.5 or 10.5 in our analysis. Relatively, this is equivalent to decreasing the velocity dispersions of massive dwarfs in level-3 by factors of 3.5 or 10.5, with respect to the level of binary motions. The scaling method enables us to effectively investigate how binary motions affect dynamical modeling outcomes for low-mass dwarfs, while at the same time maintaining a sufficient number of star particles as tracers.

In the end, we have 28 systems from level-3, which have been used in Paper I. Note that we can also use massive dwarfs in level-2 with this scaling method, but there are more massive dwarfs in level-3, as it has six MW-like systems. However, we should bear in mind that the kinematics of more massive dwarfs in AURIGA might not fully represent the kinematics of less-massive ultra-faint dwarfs, though at the current stage, the internal dynamics of ultra-faint dwarfs are not as well resolved as more massive satellites. This is currently the best approach we can adopt with AURIGA, which is so far one of the highest-resolution hydrodynamical simulations for the MW systems.

In Figure 1, we show histograms of the intrinsic LOSV dispersions for dwarf galaxies selected following the details above. Black, red, and blue histograms are level-3 systems. The black histogram shows the original velocity dispersions. The velocity dispersions of the red and blue histograms are smaller than those of the black histogram by factors of 3.5 and 10.5, respectively. With this scaling method, it is equivalent to say

[15] The virial mass, M_{200}, is defined as the mass enclosed in a radius, R_{200}, within which the mean matter density is 200 times the critical density of the Universe.

that we are investigating systems with velocity dispersions in the range of ~3–9 km s^{-1} (red histogram) and 1–3 km s^{-1} (blue histogram). In addition, the green histogram shows dwarf systems from the level-2 resolution, without any scaling to σ_{v_r}. They have velocity dispersions between 3 and 14 km s^{-1}.

Throughout this paper, the intrinsic velocity dispersions for dwarf systems in level-3 resolution will be shown after being scaled by factors of 3.5 or 10.5, and we call it the effective LOSV dispersion or $\sigma_{v_r,\mathrm{eff}}$. Note that the velocity and velocity dispersion values that we use in JAM modeling are the actual values, rather than the scaled values. What we directly scale are the part in the LOSVs due to binaries only. On the other hand, when we present the density profiles, velocity moments, and the enclosed masses within some given radius, the radial scales are still based on the original coordinates in the simulation, without any scaling. This is because it is not straightforward to figure out a universal scaling of the coordinates, after scaling the velocity dispersions. Of course, we find correlations between the velocity dispersions of star particles in dwarf satellite galaxies and the total mass or scale radius of their host subhalos in AURIGA, but the amount of scatter in the correlation is not negligible. So we choose to present the radial scales based on the original coordinates without scalings. However, the question remains: what are the approximate scaling factors in the radius, given the 10.5 and 3.5 factors of scalings in velocity dispersions? For virialized dark matter halos, the virial velocity and virial radius are proportional to each other according to the spherical collapse model (Gunn & Gott 1972). Thus, we can approximately divide the radii by factors of 10.5 or 3.5, accordingly, to obtain the rough numbers.

2.3. Mock Stars

To create mock "observed" stars in each dwarf, we start from the star particles in the simulation, and subtract from them the stellar-mass weighted mean coordinates and velocities of all bound particles belonging to each dwarf, to eliminate perspective accelerations (Feast et al. 1961). Note although each star particle is a single stellar population, we treat them as individual observed stars or unresolved binaries (see Section 2.4 for more details), i.e., we ignore the original information such as the total stellar mass or luminosity of the star particle. We place the observer on the disk plane of the host galaxy, which is defined as the plane perpendicular to the minor axis of all bound star particles with galactocentric distances smaller than 20 kpc. The observer is 8 kpc away from the galactic center, with a random position angle.

The coordinates and velocities are then transformed to the observing frame. The z'-axis of the observing frame is chosen as the line-of-sight direction. The x'-axis (major axis) is the cross product between the spin axis of the dwarf galaxy and the z'-axis, which is projected on the "sky." The y'-axis (minor axis) is the cross product between z' and x' vector, taking minus sign, which represents a left-handed observing frame (Watkins et al. 2013).

2.4. Incorporating Binary Orbital Motion

Star particles from dwarfs in the AURIGA level-3 and level-2 resolutions are used as dynamical tracers. If a star particle is determined to be a binary, its original velocity is adopted to represent the motion of the center of mass (CM), and we incorporate the binary orbital motion by sampling two orbital element distribution models based on solar neighborhood observations. The orbital elements used to determine the LOSV include the mass of the primary star, m_1, the mass ratio of the binaries, $q = m_2/m_1$, orbital period, P, orbit eccentricity, e, the inclination angle of the orbit plane, i, the argument of periapse, ω, and the true anomaly, f. In the following, we introduce their relation to the LOSV and their meanings.

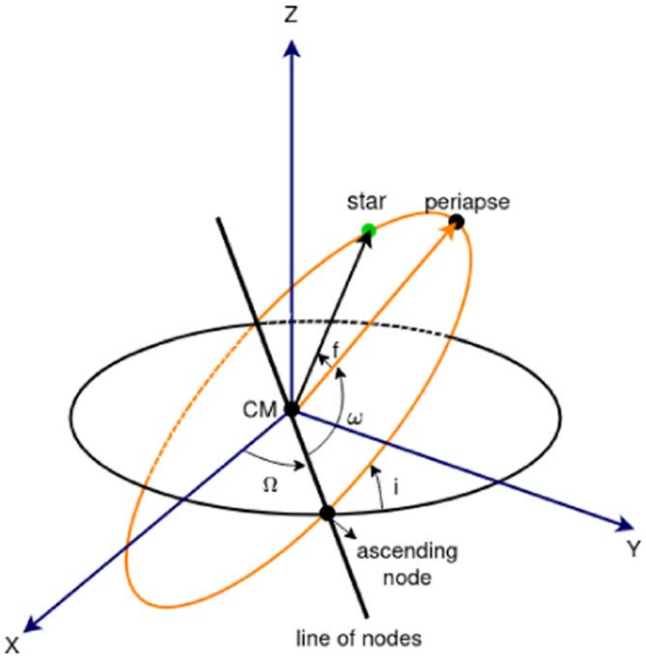

Figure 2. A demonstration of the inclination angle of the binary orbit plane (orange ellipse) with respect to the reference plane (black ellipse), i, the argument of periapse, ω, and the true anomaly, f. The origin is chosen as the center of mass (CM) of the binary system. The green dot represents the current position of the primary star. Ω is the angle between the reference line and the radius vector to the ascending node, which is not relevant for the LOSV, with the observer put at the positive Z-axis. The readers can refer to Figures 4 and 7 of Murray & Correia (2010) for similar versions of the figure.

Where m_1 and m_2 are the stellar masses of the primary and secondary stars, the LOSV of the primary star with respect to the CM is described by the following equation:

$$v_{z'} = \frac{m_2}{m_1 + m_2} \frac{2\pi a \sin i}{P\sqrt{1 - e^2}} (\cos(\omega + f) + e\cos\omega), \qquad (1)$$

where P is the orbital period, e is the orbit eccentricity, and a is the orbit major axis. a is not independent and is linked to P through $\frac{4\pi^2}{P^2}a^3 = G(m_1 + m_2)$. i is the inclination angle between the orbit plane (the orange ellipse in Figure 2) and the reference plane (the black ellipse in Figure 2), and here the reference plane is defined to be perpendicular to the line of sight (positive Z-axis of Figure 2). The line formed by the intersection of the orbit and reference planes is called the line of nodes. The ascending node is the point in both planes where the orbit crosses the reference plane moving from below to above the plane. The angle between this same radius vector and the periapse of the orbit is called the argument of periapse, ω. f is the true anomaly, which is the angle between the line connecting the periastron to the CM and the CM to the star. The binary motions with respect to the CM are thus included

through the above equation and by sampling the distributions of m_1, q, P, e, i, ω, and f.

For each star particle, we first determine whether it is a binary according to a given binary fraction ($f_{\rm binary}$). We try two different $f_{\rm binary}$, 70% and 36%. The fraction of 70% might be reached in young star-forming regions, but might not be realistic for old dwarf galaxies systems, whose binaries might have been significantly dissolved by tidal disruptions. Note that the MW field binary fraction is smaller than 50% (e.g., Minor 2013). However, in a few recent studies, fractions as high as 50%–78% were reported with high confidence levels for Draco, Ursa Minor, and Reticulum II (Spencer et al. 2018; Minor et al. 2019), and it was also shown that the binary fractions in MW dSphs can vary significantly. Thus, we try $f_{\rm binary}$ of both 70% and 36%, not only to cover a wide possibility, but also to test extreme cases.

Among the full set of orbital elements, the distribution of i, ω, and f are not model dependent. We first introduce how we sample them. The distribution of ω follows the uniform distribution over 0 and 2π, and the distribution of the inclination angle, i, is proportional to $\sin i$ in our analysis, assuming random orientation. However, observational evidence exists to show that the Oort cloud of the outer solar system shows some alignments with the Galactic disk due to the Galactic torque (e.g., Delsemme 1987; Higuchi 2020; Feng & Bailer-Jones 2014; Higuchi 2020). If the tidal torque of Galactic disk has a similar effect on binary systems in dwarf galaxies, we may expect the distribution of i to be modified. Nevertheless, the outer edge of the Oort cloud is about 10,000 to even 100,000 au from the Sun. Such a wide scale corresponds to wide binary systems with small contributions to the LOSVs (e.g., El-Badry et al. 2021; Tian et al. 2020). Additionally, most dwarf spheroids are far away from the Galactic disk, and thus their member stars are unlikely to be significantly affected by the disk torque. So we believe Galactic tidal torque would not significantly affect our analysis here.

The true anomaly, f, depends on the eccentricity and does not have analytic solution, and it does not change linearly with time. On the other hand, the mean anomaly, M, scales linearly with time. The relation between f and M is

$$M = E - e\sin E, \tag{2}$$

$$\sin f = \sqrt{1-e^2}\sin E/(1-e\cos E), \tag{3}$$

and

$$\cos f = (\cos E - e)/(1-e\cos E), \tag{4}$$

where E is the eccentric anomaly.

We first sample the mean anomaly, M, from a uniform distribution from 0–2π. E is then solved numerically through Equation (2), and in the end we solve the true anomaly, f, through Equations (3) and (4). Note that if uniformly sampling f between 0 and 2π, we end up with more epochs close to the apoastrons than it should be, which can cause the velocity dispersions to be mistakenly inflated by more than a factor of 3 (e.g., Hargreaves et al. 1996).

The distributions of m_1, q, P, and e are model dependent. In all cases, we assume the primary stars are red giants. We first fix $m_1 = 0.8\,M_\odot$ when using the AURIGA level-2 simulations for initial analysis. We then more carefully sample m_1 through the Kroupa initial mass function (IMF) corrected for binaries (Kroupa 2002), when using AURIGA level-3 simulations. The allowed mass range is determined through a 10 Gyr and solar metallicity parsec stellar evolution isochrone (Bressan et al. 2012), and to select the part for red giants, we require the surface gravity to be smaller than $\log g = 3.8$, i.e., red giants. Nevertheless, it was shown that the number of inflations in the velocity dispersion changes very little when m_1 is varied over a reasonable range (e.g., Hargreaves et al. 1996).

To sample the distributions of q, P, and e, we adopt two different models of Duquennoy & Mayor (1991) and Moe & Di Stefano (2017). The model of Duquennoy & Mayor (1991) is simple to use, and has been adopted in many studies, even recently. On the other hand, Moe & Di Stefano (2017) explicitly considered joint distributions of different orbital elements through a variety of more recent observations. Many recent studies reported prominent correlations among the distributions of different orbital elements, and thus proper modeling of the joint distributions across different orbital elements is necessary (see also, e.g., Liu 2019; Gaia Collaboration et al. 2023).

Throughout this paper, we call the orbital element distribution taken from Duquennoy & Mayor (1991) "model-I", and the distribution of Moe & Di Stefano (2017) "model-II." We briefly introduce the models in Sections 2.4.1 and 2.4.2 below.

2.4.1. Model-I

Duquennoy & Mayor (1991) modeled the distribution of mass ratio between the secondary and primary stars, $q = m_2/m_1$, through the following functional form:

$$\frac{dN}{dq} = \exp\left(-\frac{(q-\mu_q)^2}{2\sigma_q^2}\right), \tag{5}$$

where $\mu_q = 0.23$ and $\sigma_q = 0.42$.

The orbital period distribution of Duquennoy & Mayor (1991) takes the following log-normal form:

$$\frac{dN}{d\log P} = \exp\left(-\frac{(\log P-\mu_{\log P})^2}{2\sigma_{\log P}^2}\right), \tag{6}$$

where $\mu_{\log P} = 4.8$ and $\sigma_{\log P} = 2.3$. A similar distribution was reported by Raghavan et al. (2010) with $\mu_{\log P} = 5.03$ and $\sigma_{\log P} = 2.28$, which barely affects our results.

The distribution of eccentricity depends on the orbital period P and has the following form (see also Hargreaves et al. 1996):

$$\begin{aligned} &e = 0,\ P < 11 \text{ days};\\ &\frac{dN}{de} = \exp\left(\frac{-(e-0.3)^2}{0.16^2}\right),\ 11 \text{ days} < P < 1000 \text{ days};\\ &\frac{dN}{de} = 2e,\ P > 1000 \text{ days}. \end{aligned} \tag{7}$$

When adopting model-I, we try different sampling of m_1 and $f_{\rm binary}$: (1) $m_1 = 0.8\,M_\odot$ and $f_{\rm binary}$ of 70% (model-Ia); (2) m_1 sampled from Kroupa IMF and $f_{\rm binary}$ of 70% (model-Ib); and (3) m_1 sampled from Kroupa IMF and $f_{\rm binary}$ of 36% (model-Ic). Note when we apply model-Ib and model-Ic to level-3 simulations, the incorporated binary orbital motions are scaled up by a factor of 3.5.

2.4.2. Model-II

The more recent study of Moe & Di Stefano (2017) provides the joint distribution of P, q, and e over a wide stellar-mass range of main-sequence stars, though in old dwarf galaxies, massive stars should have died out, and the red giants used as tracers have solar mass.

The mass ratio distribution is modeled as

$$\frac{dN}{d\log q} \propto q^{\gamma}, \tag{8}$$

where

$$\gamma = \begin{cases} \gamma_{\rm small}, & 0.1 < q < 0.3; \\ \gamma_{\rm large}, & 0.3 < q < 1. \end{cases} \tag{9}$$

The functional form of $\gamma_{\rm small}$ and $\gamma_{\rm large}$ depends on both m_1 and the orbital period, P. The readers can refer to Moe & Di Stefano (2017) for details, and we do not repeat the exact forms here. Note that Moe & Di Stefano (2017) also explicitly considered the excess probability of twin binaries with mass ratios very close to unity and on the basis of Equation (9), but when we sample the distribution of q, we did not consider the excess twin binary fraction. This is because at late evolutionary stages, twin binaries likely have their radii exceeding the Roche-lobe size, and thus it is unlikely that there is a large fraction of twin binaries in old dwarf systems.

The orbital period distribution of P depends on both m_1 and q, which is split into two parts, $0.1 < q < 0.3$ and $0.3 < q < 1$. At $q > 0.3$, the distribution depends on m_1, with analytical expression provided by the original paper, which we do not repeat. At $0.1 < q < 0.3$, the period distribution is determined by the distribution at $q > 0.3$ and Equation (9). For example, if $\frac{dN}{d\log P} = 0.14$ at $q > 0.3$ and $\gamma_{\rm small} = \gamma_{\rm large} = 0$, we have $\frac{dN}{d\log P} = 0.18$ at $q > 0.1$. Here the period distribution at $P > 0.1$ is the summation of the distributions at $P > 0.3$ and $0.1 < P < 0.3$.

The distribution of the orbital eccentricity, e, is modeled as

$$\frac{dN}{d\log e} \propto e^{\eta}, \tag{10}$$

where η depends on both m_1 and P. We do not repeat the formula here, and the readers can check Moe & Di Stefano (2017) for the detailed expression.

According to Moe & Di Stefano (2017), given m_1 and P, the maximum eccentricity is $e_{\rm max}(P) = 1 - \left(\frac{P}{2\ {\rm days}}\right)^{-2/3}$, which guarantees the binaries to have Roche-lobe fill-factors $<\sim$70% at periastron.

For model-II, we sample m_1 from the Kroupa IMF only, but we adopt the binary fractions of both 70% (model-IIa) and 36% (model-IIb). The fraction of 36% is in fact the integrated binary fraction for solar-mass binaries by Moe & Di Stefano (2017).

For model-Ia, model-Ib, model-Ic, model-IIa, and model-IIb, we do not include observational errors. On the basis of model-IIa and model-IIb, we will additionally include a typical observational error of 3 km s^{-1} to the LOSVs of mock stars. This is achieved by shifting the "observed" velocities (original + binary motions) by an amount sampled from a Gaussian distribution with zero mean and 3 km s^{-1} of scatter. The models are then called model-IIa-err and model-IIb-err. Furthermore, on the basis of model-IIa-err and model-IIb-err, we will discard tracer stars whose changes in their LOSVs are greater than 5 km s^{-1} in two observations over 1 yr. This is because stars with large changes in their LOSVs are likely binaries, and here we want to investigate the efficiency of using two epoch observations to exclude binaries given different models and observational errors. We call them model-IIa-2epoch and model-IIb-2epoch. Note for the 1 yr separation between the two observations, we did not apply any scaling.

Note the binary orbital motions of model-Ib, model-Ic, model-IIa, model-IIb, model-IIa-err, model-IIb-err, model-IIa-2epoch, and model-IIb-2epoch are all scaled up by a factor of 3.5. This enables us to effectively investigate intrinsic velocity dispersions of $3 < \sigma_{v_r,{\rm eff}} < 9$ km s^{-1}. In the end and in order to investigate the range of $1 < \sigma_{v_r,{\rm eff}} < 3$ km s^{-1}, we try models in which we scale the binary motions by a factor of 10.5. The models are included on the basis of model-IIa-2epoch and model-IIb-2epoch, and are denoted "model-IIa-FD" and "model-IIb-FD." Here, "FD" stands for "Faint enD." Their orbital element distribution model and binary fractions are all the same as model-IIa and model-IIb, but we have excluded stars whose changes in their LOSVs are greater than 5 km s^{-1} in two observations over 1 yr. Additionally, for model-IIa-FD and model-IIb-FD, we incorporate observational errors of 1 km s^{-1} instead of 3 km s^{-1}. This is because we are investigating 1–3 km s^{-1} of region with this model, and 3 km s^{-1} of error is too large, i.e., cannot enable reasonable dynamical constraints for dwarfs with intrinsic velocity dispersions between 1 and 3 km s^{-1}.

In both model-I and model-II, we require the stellar radius to be smaller than the Roche radius. The stellar radius is estimated from the effective temperature and the luminosity of a 10 Gyr and solar metallicity parsec stellar evolution isochrone. The Roche radius is calculated from the analytical formula of Eggleton (1983) at periastron, with a correction for a weak dependence on orbital eccentricity (Minor et al. 2010). This is an important step, which eliminates a significant fraction of close binaries with small orbital periods and high orbital velocities.

In Table 1, we summarize the models used to sample binary orbital motions. In particular, for model-Ib, model-Ic, and all model-II, we include 3σ clippings to exclude stars with extreme velocities, after including the binary orbital motions. For models with observational errors, 3σ clippings are achieved after including errors. However, for initial checks with model-Ia applied to level-2 suite of simulations, we did not include such 3σ clippings.

2.5. Mock Dwarf Images and Multi-Gaussian Expansion

In our dynamical modeling approach (see Section 3 for details), the potential and density distributions of the luminous stellar component will be directly inferred from the optical images of the dwarfs, with the stellar-mass-to-light ratios (M/L) being free parameters. The image will be deprojected based on the distance and inclination angle of the dwarf. The inclination angle and the distance of the dwarf can be free parameters, but in our case, we fix them to the true values.

Thus, we need to create mock images for our sample of dwarfs. We simply adopt the projected stellar-mass density distribution to create the images, i.e., the read in each pixel is in units of $M_\odot/{\rm pc}^2$ based on all bound star particles associated to the dwarf galaxy; so in our case, the true value of M/L is unity.

Table 1
Models Adopted for Sampling Binary Orbital Motions

Model	Reference	$f_{\rm binary}$ (%)	m_1 ($M_\odot$)	Clipping	Resolution	Error (km s^{-1})	Epoch
model-Ia	Duquennoy & Mayor (1991)	70	0.8	no	level-2	no	1
model-Ib	Duquennoy & Mayor (1991)	70	Kroupa IMF	yes	level-3	no	1
model-Ic	Duquennoy & Mayor (1991)	36	Kroupa IMF	yes	level-3	no	1
model-IIa	Moe & Di Stefano (2017)	70	Kroupa IMF	yes	level-3, 3.5 scaling	no	1
model-IIb	Moe & Di Stefano (2017)	36	Kroupa IMF	yes	level-3, 3.5 scaling	no	1
model-IIa-err	Moe & Di Stefano (2017)	70	Kroupa IMF	yes	level-3, 3.5 scaling	3	1
model-IIb-err	Moe & Di Stefano (2017)	36	Kroupa IMF	yes	level-3, 3.5 scaling	3	1
model-IIa-2epoch	Moe & Di Stefano (2017)	70	Kroupa IMF	yes	level-3, 3.5 scaling	3	2
model-IIb-2epoch	Moe & Di Stefano (2017)	36	Kroupa IMF	yes	level-3, 3.5 scaling	3	2
model-IIa-FD	Moe & Di Stefano (2017)	70	Kroupa IMF	yes	level-3, 10.5 scaling	1	2
model-IIb-FD	Moe & Di Stefano (2017)	36	Kroupa IMF	yes	level-3, 10.5 scaling	1	2

Note. In the second column, we provide the references for the binary orbital element distributions, which are used to sample the changes in line-of-sight velocities (LOSVs) due to binary motions. We also summarize for each model the binary fraction ($f_{\rm binary}$), how the stellar mass of the primary star is sampled, whether 3σ clipping is applied to the "observed" LOSVs, the resolution of the AURIGA simulation to which the model is applied, whether observational errors are incorporated, and whether we discard star particles whose change in their LOSVs are greater than 5 km s^{-1} based on two epoch "observations" spanning 1 yr.

Once the mock images are made, the luminous stellar-mass distribution, $\Sigma(x', y')$, will be decomposed to a few different Gaussian components (multi-Gaussian expansion, or MGE in short), in order to enable the analytical deprojection for any arbitrary $\Sigma(x', y')$ and to bring analytical solutions for any arbitrary matter distribution (see Section 3 and Paper I for more details).

3. Methodology

Jeans Anisotropic Multi-Gaussian Expansion (JAM) is a public source of code.[16] It is a powerful tool to constrain both the underlying matter distribution and the internal dynamics of tracers (e.g., Zhu et al. 2016b, 2016a), based on either LOSVs or proper motions of tracers. In this paper, we will only use the LOSVs for dynamical modeling. The version of JAM we use is slightly different from the public version of the JAM model for discrete data Watkins et al. (2013), with improved python interface and plotting tools. Details about JAM can be found in Cappellari (2008) and Watkins et al. (2013), and here we only briefly introduce the method.

The method is based on solving the axisymmetric Jeans equation in an intrinsic frame defined on the dwarf galaxy with cylindrical coordinates, to solve for the first and second velocity moments.

$$\frac{\nu(\overline{v_R^2} - \overline{v_\phi^2})}{R} + \frac{\partial \nu \overline{v_R^2}}{\partial R} + \frac{\partial \nu \overline{v_R v_z}}{\partial z} = -\nu \frac{\partial \Phi}{\partial R} \tag{11}$$

$$\frac{\nu \overline{v_R v_z}}{R} + \frac{\partial \nu \overline{v_R v_z}}{\partial R} + \frac{\partial \nu \overline{v_z^2}}{\partial z} = -\nu \frac{\partial \Phi}{\partial z}, \tag{12}$$

where ν is the tracer density distribution. Φ is the total potential. Upon solving the equation to obtain unique solutions, the cross velocity terms are assumed to be zero, i.e., $\overline{v_R v_z} = 0$. In addition, the anisotropy parameter, b, is assumed to be constant and defined as $\overline{v_R^2} = b\overline{v_z^2}$. A rotation parameter, κ, is introduced as $\overline{v_\phi} = \kappa(\overline{v_\phi^2} - \overline{v_R^2})^{1/2}$.

In our analysis, we define the z-axis of the intrinsic frame as the direction of the averaged spin of all bound star particles to the dwarf in the simulation, and the intrinsic frame is a right-handed system. The intrinsic frame is linked to the observing frame (see Section 2.3 above) through the inclination angle, i, of the dwarf galaxy

$$\begin{pmatrix} x' \\ y' \\ z' \end{pmatrix} = \begin{pmatrix} 1 & 0 & 0 \\ 0 & -\cos i & \sin i \\ 0 & \sin i & \cos i \end{pmatrix} \begin{pmatrix} x \\ y \\ z \end{pmatrix}, \tag{13}$$

and

$$\begin{pmatrix} v_{x'} \\ v_{y'} \\ v_{z'} \end{pmatrix} = \begin{pmatrix} \cos i & -\sin i & 0 \\ \sin i & \cos i & 0 \\ 0 & 0 & 1 \end{pmatrix} \begin{pmatrix} v_R \\ v_\phi \\ v_z \end{pmatrix}, \tag{14}$$

where $R = \sqrt{x^2 + y^2}$.

The total potential, Φ, on the right-hand side of Equations (11) and (12), is contributed by both luminous and dark matter. As we have mentioned, the luminous matter distribution is directly inferred from the surface brightness of the dwarf galaxy (see Section 2.5 above). To model the density profile of dark matter, we adopt in our analysis a double power-law functional form of

$$\rho(r) = \frac{\rho_s}{(r/r_s)^\gamma (1 + r/r_s)^\alpha}, \tag{15}$$

with the model parameters (ρ_s, r_s, and γ) constrained. Note that in our analysis throughout this paper, the outer power-law index, α, will be fixed to 3.

In order to have analytical solutions for any given potential model and tracer distribution, MGE is not only applied to the two-dimensional surface density distribution of the luminous stellar component (see Section 2.3 above), but also to the underlying model for the dark matter distribution and to the density distribution of tracers (ν) as well.[17] Each MGE component would have analytical solutions to Equations (11) and (12). In principle, each MGE component of the tracer population can have its own rotation parameter, κ_k, and velocity anisotropy parameter, b_k. M/L for each MGE

[16] https://github.com/lauralwatkins/cjam

[17] In our case, tracers and the luminous stellar component have the same distribution, and therefore the same MGEs. Note that the normalization of the MGE components for tracers is not important, which cancels out on two sides of the equations.

component can also differ, but in our analysis, we treat κ, b, and M/L to be the same for different MGEs.

For an observed star with position $\boldsymbol{x'}_i = (x'_i, y'_i)$ on the image plane, which has observed velocity $\boldsymbol{v}_i = (v_{x',i}, v_{y',i}, v_{z',i})$ and error matrix of

$$\boldsymbol{S}_i = \begin{pmatrix} \sigma^2_{v_{x'},i} & 0 & 0 \\ 0 & \sigma^2_{v_{y'},i} & 0 \\ 0 & 0 & \sigma^2_{v_{z'},i} \end{pmatrix}, \tag{16}$$

its position, $\boldsymbol{x'}_i$, can be transformed to the intrinsic frame to solve the corresponding velocities and velocity dispersions, based on a set of model parameters, Θ. A solution for each MGE is sought, and solutions of different MGEs are added together in the end. The solutions are then transformed back to the observing frame. The mean velocity predicted by the model in the observing frame is denoted as $\boldsymbol{\mu}_i = (v_{x',i}, v_{y',i}, v_{z',i})$, and the covariance matrix is defined through both the first and the second velocity moments

$$\boldsymbol{C}_i = \begin{pmatrix} \overline{v^2_{x',i}} - \overline{v_{x',i}}^2 & \overline{v^2_{x'y',i}} - \overline{v_{x',i}}\,\overline{v_{y',i}} & \overline{v^2_{x'z',i}} - \overline{v_{x',i}}\,\overline{v_{z',i}} \\ \overline{v^2_{x'y',i}} - \overline{v_{x',i}}\,\overline{v_{y',i}} & \overline{v^2_{y',i}} - \overline{v_{y',i}}^2 & \overline{v^2_{y'z',i}} - \overline{v_{y',i}}\,\overline{v_{z',i}} \\ \overline{v^2_{x'z',i}} - \overline{v_{x',i}}\,\overline{v_{z',i}} & \overline{v^2_{y'z',i}} - \overline{v_{y',i}}\,\overline{v_{z',i}} & \overline{v^2_{z',i}} - \overline{v_{z',i}}^2 \end{pmatrix}. \tag{17}$$

By assuming the velocity distribution predicted by the model is a tri-variate Gaussian with mean velocity $\boldsymbol{\mu}_i$ and covariance $\boldsymbol{C}_i$ at $\boldsymbol{x'}_i$, the likelihood can be written as

$$\begin{aligned} L_i^{\rm dwarf} &= p(\boldsymbol{v}_i|\boldsymbol{x'}_i, \boldsymbol{S}_i, \Theta) \\ &= p(\boldsymbol{v}_i|\boldsymbol{x'}_i, \boldsymbol{S}_i, \boldsymbol{\mu}_i, \boldsymbol{C}_i) \\ &= \frac{\exp\left[-\frac{1}{2}(\boldsymbol{v}_i - \boldsymbol{\mu}_i)^{\rm T}(\boldsymbol{C}_i + \boldsymbol{S}_i)^{-1}(\boldsymbol{v}_i - \boldsymbol{\mu}_i)\right]}{\sqrt{(2\pi)^3|(\boldsymbol{C}_i + \boldsymbol{S}_i)|}}. \end{aligned} \tag{18}$$

The total likelihood is the product of the likelihood for each star

$$L = \prod_{i=1}^{N_{\rm star}} L_i. \tag{19}$$

Note, however, in our case, we only use the LOSV information, while the information of $v_{x',i}$ and $v_{y',i}$ are not available. We simply set $v_{x',i} = v_{y',i} = 0$ and input very large values for $\sigma^2_{v_{y'},i}$ and $\sigma^2_{v_{z'},i}$. This is equivalent to only fit the observed first and second moments of LOSVs.

The list of parameters used in our modeling are summarized as follows:

1. Rotation parameter, κ;
2. Velocity anisotropy, b;
3. Dark matter halo scale density, ρ_s;
4. Dark matter halo scale radius, r_s;
5. Inner density slope of the host dark matter halo, γ.

In Paper I, we have reported strong degeneracies between the stellar and dark matter components, and thus M/L is poorly constrained for our sample of dwarf galaxies. Observationally, M/L can be alternatively constrained through stellar population synthesis modeling and then fixed upon dynamical modeling. Hence in our analysis through this paper, the stellar-mass-to-light ratio, M/L, will simply be fixed to unity, i.e., its true value. We also fix the distance and the inclination angle to be their true values. Moreover, the outer density slope, α, will be fixed to 3, but we have also tried to vary the outer slopes, and our conclusions are not sensitive to α.

4. Results

4.1. Model-Ia Applied to Level-2 Resolution

We first show results based on 17 dwarf galaxies selected from the level-2 suite of AURIGA simulations. The results in this current subsection are based on model-Ia. Figure 3 shows the best-constrained masses by JAM (y-axis) versus the true masses (x-axis). In the two panels, the true masses along the x-axis are exactly the same, whereas the JAM constrained masses are based on the original LOSVs of star particles and the LOSVs after including binaries, for the left and right panels, respectively. Red circles represent the masses between 100 and 200 pc, M(100–200pc), and black squares refer to the masses within the half-mass radius of tracer stars, $M(< r_{\rm half})$. Note that the softening scale of AURIGA level-2 resolution is only slightly smaller than 100 pc, and the deviation from the Newtonian gravitational potential starts to become important within the quoted softening scale (Springel 2010).

The $y = x$ diagonal dashed lines are to guide the eye, and are exactly the same in both panels. For massive dwarfs, there is no prominent difference between the best-constrained mass in the two panels. However, for the few red circles and black squares at the low-mass end, their JAM constrained masses along the y-axis are prominently higher after including binary orbital motions in the right panel than the left one. This indicates such low-mass systems are more likely to be significantly affected by binaries upon dynamical constraints.

In the right panel, we further mark the total stellar mass of different dwarf systems. Symbols overplotted with cyan triangles, green squares, and blue stars represent dwarf systems with total stellar mass in the ranges of $10^{6-7.5}\,M_\odot$, $10^{5-6}\,M_\odot$, and $10^{4-5}\,M_\odot$, respectively. Despite the fact that the blue stars have the smallest total mass, they span a wide range in $M_{\rm fit}$(100–200 pc) and $M_{\rm fit}(< r_{\rm half})$. It is not really the total stellar mass matters, but instead, the amount of inflation for the mass within a given radius is more closely related to the velocity dispersion at the corresponding radius.

In both panels, the symbols distribute more or less symmetrically around the $y = x$ diagonal line, indicating the best-fitting dynamical mass is ensemble unbiased. However, at the low-mass end of the left panel, the few red circles are prominently lower than the diagonal line, indicating systematic underestimates in the dynamical mass compared to reality. After including binaries, the few red circles at the low-mass end go more symmetrically around the diagonal line. We think the underestimates in the left panel could be related to the softening scale of the level-2 resolution. Although 100–200 pc is greater than the softening scale of level-2, the half-light radius of such low-mass dwarfs is a few hundred parsecs (Grand et al. 2021), with an average of $\sim$300 pc at $10^{4-5}\,M_\odot$. The softening scale is significant compared with the dwarf size, and thus internal dynamics of star particles for such low-mass dwarf galaxies is likely still affected above the softening length. Moreover, such low-mass level-2 dwarf systems have only a few tens of star particles, which could be more vulnerable to the resolution limit. The inclusion of binary motions, on the other hand, boost

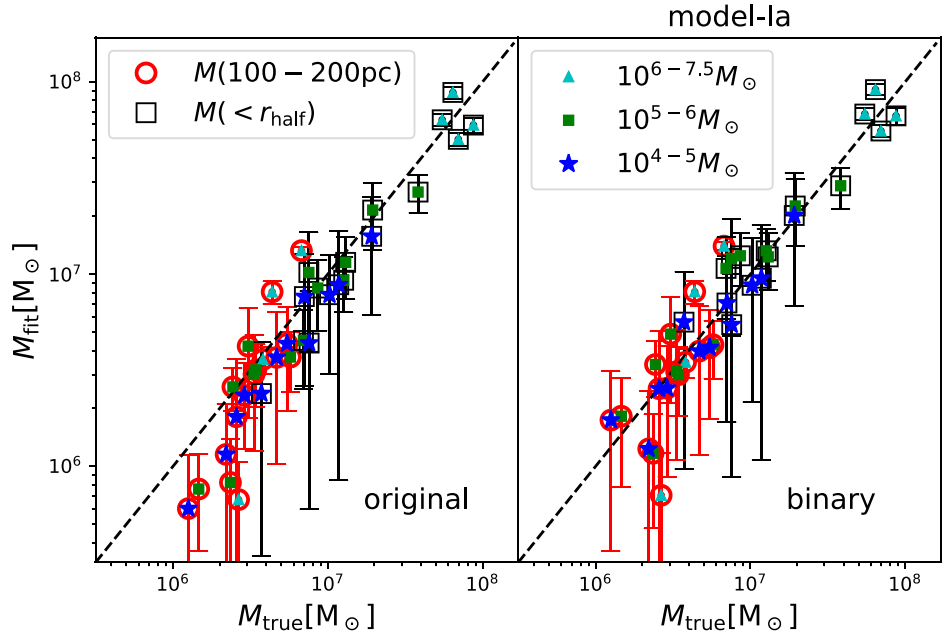

Figure 3. Best-fitting vs. true mass, for the total masses enclosed within the half-mass radius of tracers (black square, $M(<r_{\mathrm{half}})$) and the masses between 100–200 pc (red circles, M(100–200 pc)). This is shown for 17 dwarf systems selected from the AURIGA level-2 simulations. Results in the left panel are dynamical constraints based on the true velocities of tracer star particles in the simulation, while results in the right panel are based on the velocities after incorporating binary orbital motions (model-Ia). In both panels, the diagonal black dashed line marks $y = x$ to guide the eye. Error bars are 1σ statistical errors of the best fits. In the left panel, most measurements are ensemble unbiased, which distribute symmetrically around the black dashed line. However, at the low-mass end of the left panel, the best-fitting masses are significantly underestimated, which could be either due to the small tracer sample size or due to the softening scale limit. In the right panel, red circles or black squares overplotted with cyan triangles, green squares, and blue stars are dwarf galaxies with different total stellar masses, as indicated by the legend.

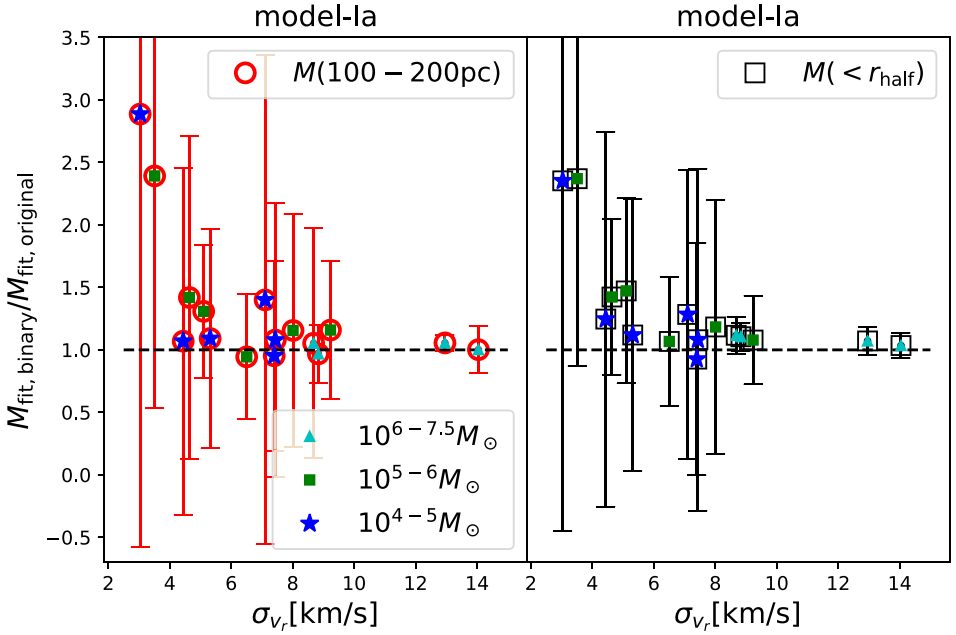

Figure 4. The ratios between best-fitting total masses after and before including binary motions of model-Ia (y-axis), reported as a function of the intrinsic LOSV dispersions of the dwarf systems (x-axis). We show the total masses enclosed within the half-mass radius of tracers (black square, left panel; $M(<r_{\mathrm{half}})$) and the masses between 100 and 200 pc (red circles, right panel; M(100–200 pc)). This figure is based on 17 dwarf systems from the AURIGA level-2 simulations. Red circles or black triangles with cyan triangles, green squares, and blue stars are dwarf galaxies with different total stellar masses, as indicated by the legend. Error bars are 1σ statistical errors of the best fits.

the best-constrained dynamical mass. The boosted dynamical masses better go through the $y = x$ diagonal line at the low-mass end, which could just be a coincidence due to the coaddition of two effects.

Despite the possible effect by the resolution limit, the difference between the left and right panels at the low-mass end due to binaries is real and robust. Figure 4 further shows the ratios between the JAM constrained dynamical masses, after and before the inclusion of binaries. The ratios are reported as a function of the intrinsic LOSV dispersions of the dwarfs (without binary). The left and right panels show M(100–200pc) and $M(<r_{\mathrm{half}})$, respectively. There exists a prominent trend

that with the decrease in σ_{v_r}, the binary motions tend to introduce larger inflations in the best-constrained dynamical masses. At $\sigma_{v_r} \sim 3\,\mathrm{km\,s^{-1}}$, the amount of boost in M (100–200pc) or $M(<r_{\rm half})$ based on model-Ia can be a factor of 2.5. Note, however, this factor of 2.5 is without 3σ clippings of the observed LOSVs. After 3σ clippings, it gets much smaller. Unfortunately, we have only a few tens of star particles as tracers here, so the associated error bars are very large.

To summarize, Figures 3 and 4 unambiguously show us the effect of how binary orbital motions boost the best-constrained dynamical mass of dwarf galaxies at low σ_{v_r}. With a few tens of star particles as tracers, the trends are prominent at the low-mass end. However, such a small number of tracers lead to large statistical errors, and the dynamical mass seems to be affected by the resolution limit for such low-mass systems. These make the results hard to interpret. Thus, in the following subsections, we move on to show results based on larger samples of tracer star particles from more massive dwarf galaxies of the AURIGA level-3 simulations, with a scaling method to manually increase the level of binary motions.

4.2. Model-Ib and Model-Ic Applied to Scaled Level-3 Resolution

As we have discussed in Section 2.4, the AURIGA level-3 resolution is not high enough to bring a sufficient number of tracer star particles for decent dynamical modelings of $10^{4-5}\,M_\odot$ dwarf systems. Thus, in this subsection, we combine level-3 with a scaling method. Though the resolution of level-3 is even lower, we manually increase the binary orbital motions by a factor of 3.5, while incorporating binary motions to level-3 dwarf systems more massive than $10^{7.5}\,M_\odot$. This is equivalent to having decreased σ_{v_r} of level-3 massive dwarf systems by a factor of 3.5, and thus we can investigate the effect of binary motions on dwarf systems with effective LOSV dispersions, $\sigma_{v_r,\rm eff}$, in the range of 3–9 $\mathrm{km\,s^{-1}}$ (see the distributions in Figure 1), and at the same time we have enough number of star particles to be used as tracers.

After applying model-Ib to 28 such dwarf systems from level-3, the results are shown in Figure 5. Similar to Figure 4, the y-axis demonstrates the ratios between the JAM constrained dynamical masses after and before including binary motions, which are reported as a function of the intrinsic $\sigma_{v_r,\rm eff}$ of the host dwarf systems. Red dots and black squares refer to the total masses between 200 and 300 pc, M(200–300 pc), and $M(<r_{\rm half})$, respectively, but now they are shown in the same panel. Here, the softening scale of level-3 resolution is close to 200 pc at $z=0$; so instead of plotting M(100–200 pc), we adopt M(200–300 pc).

Here we only show the ratios between the best-constrained masses before and after including binaries. Regarding the performance of JAM without including binaries, as compared to reality in the simulation, we refer the reader to Paper I for details, in which we performed very detailed comparisons of the best-fitting mass profiles by JAM and in reality. In short, we find ensemble unbiased best fits with respect to reality, with a scatter of 0.167 dex in M(200–300 pc) for the 28 systems from the level-3 resolution.

In order to control the size of statistical errors, we use all available star particles in these dwarf systems, if the total number of bound star particles is smaller than 20,000. If the total number of star particles is greater than 20,000, we randomly draw a subsample of 20,000, in order to control the time cost in a reasonable range.

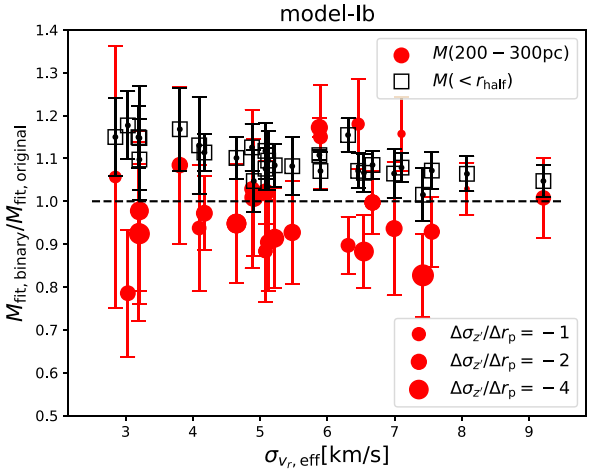

Figure 5. The ratios between best-fitting total masses after and before including binary motions of model-Ib (y-axis), reported as a function of the intrinsic effective LOSV dispersions of the dwarf systems (x-axis). We show the total masses enclosed within the half-mass radius of tracers (black square, $M(<r_{\rm half})$) and the masses between 200 and 300 pc (red dots, M(200–300 pc)). The assumed $f_{\rm binary}$ is 70%. This figure is based on 28 dwarf systems from the AURIGA level-3 simulations, after scaling the LOSVs by a factor of 3.5 to represent low-mass dwarf galaxies (see Section 2.2 for details). Note that the radial scales (200 and 300 pc) are based on original coordinates from the simulation, which are not scaled. The size of the red dots is inversely proportional to the averaged radial gradient of the intrinsic LOSV dispersion profile over $0.2r_{\rm half}$ and $2r_{\rm half}$ (binaries not included). The more negative the gradients are, the larger the symbol sizes. Dwarfs with M(200–300 pc) deflated are more likely to have more negative radial gradients in their velocity dispersion profiles. Error bars are 1σ statistical errors of the best fits.

Now with the statistical errors controlled smaller, we can clearly see the black squares deviating from unity. With the decrease in the intrinsic $\sigma_{v_r,\rm eff}$, the dynamically constrained $M(<r_{\rm half})$ is more significantly inflated, reaching maximums of ∼15% at $\sigma_{v_r,\rm eff} \sim 3\,\mathrm{km\,s^{-1}}$. With $f_{\rm binary}$ as high as 70%, the dynamically constrained $M(<r_{\rm half})$ can be inflated by ∼4% even at velocity dispersion of 9 $\mathrm{km\,s^{-1}}$, though the lower error bar touches ∼1%. Between 5 and 8 $\mathrm{km\,s^{-1}}$, the number of inflations are ∼6%–11%. Note that, herein, 3σ clippings have been applied to the observed LOSVs, so at the low $\sigma_{v_r,\rm eff}$ end, the number of inflations is significantly smaller than those in Figure 4.

Compared with the black squares, the behavior of red dots is quite different in Figure 5. Surprisingly, when all black squares are above unity, we can see a large fraction of red dots are in fact below unity. In other words, instead of showing inflations after including binary motions, M(200–300 pc) are more likely *deflated*. Moreover, although $M(<r_{\rm half})$ are inflated more with the decrease in $\sigma_{v_r,\rm eff}$, the number of deflations in M (200–300 pc) does not show prominent dependence on $\sigma_{v_r,\rm eff}$. For dwarf galaxies with $\sigma_{v_r,\rm eff}$ of 5–8 $\mathrm{km\,s^{-1}}$ and if their M (200–300 pc) are deflated due to binary motions, the number of deflations is up to ∼10%–20%.

In order to investigate the reasons why M(200–300 pc) are more likely deflated after including binary motions, we show in the left and middle plots of Figure 6 the dynamically constrained density profiles before and after including binary motions, for example, two dwarf systems, Au21-17 and Au27-19. The two systems correspond to the symbols with the smallest $\sigma_{v_r,\rm eff}$ in Figure 5 (the two leftmost red dots). Here,

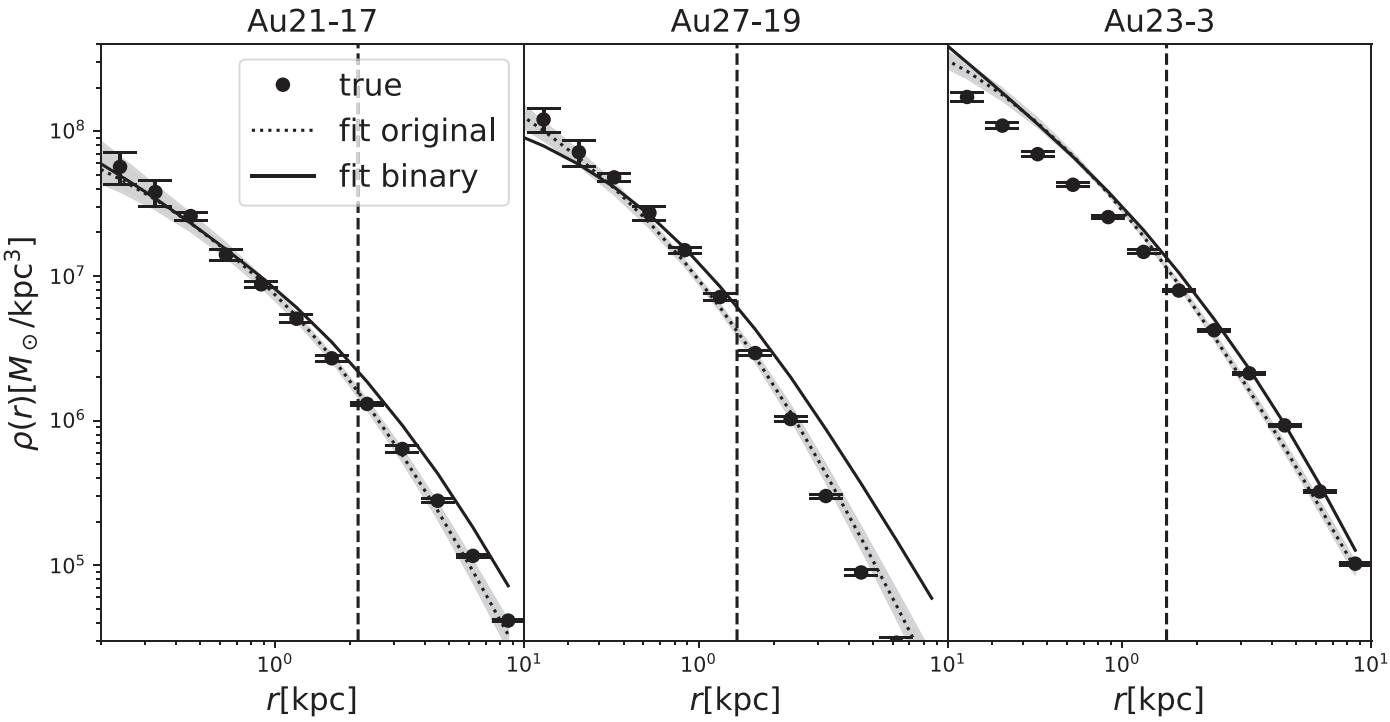

Figure 6. Black dots with error bars are true total density profiles in three example dwarf systems from the level-3 resolution of AURIGA, Au21-17 (left), Au27-19 (middle), and Au23-3 (right). The error bars are the 1σ scatters of 100 bootstrapped samples. Black dotted lines are JAM constrained density profiles from stellar dynamics, with the black shaded region reflecting the 1σ uncertainty region. Black solid lines are JAM constrained density profiles after including binary orbital motions from model-Ib. The errors of the black solid lines are similar to those of black dotted lines, and are thus not shown. In the right plot, the inflation in M (200–300 pc) is greater than the inflation in $M(< r_{\rm half})$, which is likely due to the few number of tracer star particles in the center and statistical fluctuations. Note that the x-axis radius is based on original coordinates from the simulation, which are not scaled. In all three panels, the vertical dashed line indicates the position of $r_{\rm half}$.

Au21-17 has its M(200–300 pc) inflated (red circle above unity though with large errors), and Au27-19 has its M(200–300 pc) deflated (red circle below unity) after including binary motions. Note that although we show the example density profiles for two dwarf systems only, the same trend holds for other dwarf galaxy systems from level-3.

In the left plot of Figure 6, though the solid curve is above the dotted curve at all radii, the difference is greater at larger radii, which gradually becomes smaller in inner regions. In the middle plot, the solid curve is lower in amplitude than the dotted curve within ∼350 pc, but at larger radii, the solid curve is above the dotted one. It seems that the number of inflations is more significant in the outskirts, whereas it decreases significantly in inner regions, which even turns into deflations at the very center.

The above trend is due to the negative radial gradients in the velocity dispersion profiles of realistic dwarf galaxy systems. In Figure 7, we show the LOSV and LOSV dispersion profiles for Au21-17 and Au27-19. After including binary motions, the first moments do not show any significant systematic differences, and the second moments are boosted. However, the LOSV dispersions significantly decrease with the increase in radii. As a result, the fractional inflations in the LOSV dispersion due to binary motions are more prominent in outskirts.

Now we clearly see that the velocity dispersions show strong radial dependences. This would also cause radius-dependent biases due to binary motions in dynamical constraints. The number of intrinsic dispersions is significantly lower at larger radius, and thus σ_{v_r} and the best-constrained dynamical masses are likely to be inflated more. The larger inflations in σ_{v_r} lead to higher density profiles in the outskirts, whereas the smaller inflations in σ_{v_r} and in central regions do not lead to as significant increases in the best-fitting density profiles. This explains why the black solid curves are higher above the black dotted curves in the outskirts of Figure 6, whereas the difference is much smaller in the central regions, even with switched trends. In better fitting to the outskirts, the central density profiles can even be underestimated after including binary motions. As a result, we see that many red dots are below unity in Figure 5. Moreover, since dwarf systems investigated in this study all have such negative radial gradients in their velocity dispersion profiles, this perhaps answers why the deflations in M(200–300 pc) do not show strong dependences on σ_{v_r}.

The size of the red dots in Figure 5 is chosen to be inversely proportional to the averaged radial gradient of the intrinsic[18] LOSV dispersion profile over $0.2r_{\rm half}$ and $2r_{\rm half}$. Explicitly, the more negative the gradients in the LOSV dispersion profiles are, the larger the symbol sizes. Note that when calculating the gradients in the LOSV dispersion profiles, we draw circles in the plane perpendicular to the LOS direction, instead of distinguishing the major and minor axes as in Figure 7. We can see that for dwarfs with M(200–300 pc) deflated, they are indeed more likely to have more negative radial gradients in their LOSV dispersion profiles. This supports our explanation above.

However, we anticipate that the reader may have concern over our choice of radial range (200–300 pc) being close to the softening scale in AURIGA level-3 (slightly below 200 pc), which is marginal. Is it possible that the deflations are affected by the softening? We thus try a different choice of radial range

[18] Using the gradients of the LOSV dispersion profiles after including binaries leads to very similar conclusions.

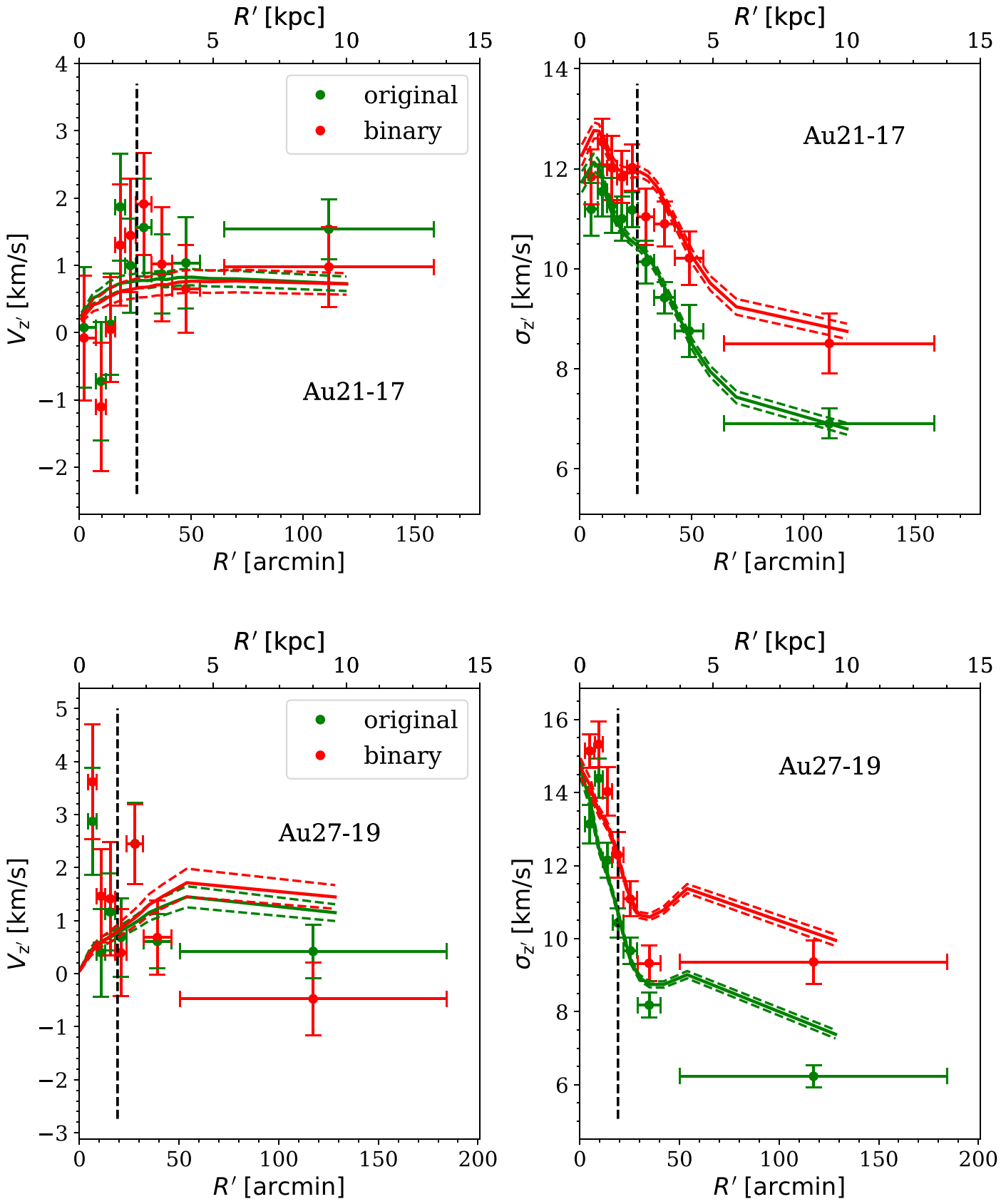

Figure 7. The first (left panels) and second (right panels) moments of the LOSVs along the major axes of Au21-17 (top) and Au27-19 (bottom). In all plots and panels, the green and red dots are velocity moments based on star particles within sectors of ±45° to the major axes. Each bin contains 200 stars. Binary orbital motions are not included for green dots, and are included for red dots. Solid curves with corresponding colors are the best fits by JAM, with dashed curves around the solid ones showing the 1σ uncertainties of the best-fitting models. Note that in both plots, the velocity dispersions are the intrinsic values from the simulations and are not scaled. The vertical black dashed lines mark the positions of $r_{\rm half}$.

(300–400 pc), and find the correlations between the gradients in the LOSV dispersion profiles and the numbers of inflations/deflations in M(300–400 pc) still exist. This supports our argument that the deflations are due to the shape of the velocity dispersion profiles, rather than due to numerical effects. Moreover, if there exist any deviations from Newtonian on small scales, the effect is very likely the same before and after including binaries, which is not expected to violate our conclusion.

There are a few red dots that are above the black squares in Figure 5. These are very likely statistical fluctuations due to the small number of tracer star particles in the very center of these systems, because these red dots still marginally agree with the black squares within 1σ errors. One example density profile is shown in the right plot of Figure 6 (Au23-3). We can see the black solid line (best fit after including binaries) goes higher above the dotted line at large radius, and the black and dotted lines gradually becomes more similar at smaller radius. In the very center, the black line starts to turn up again, but the errors also become significantly larger.

Note that a similar trend was not seen for the red circles in Figure 4. This is mainly because at the low $\sigma_{v_r,\mathrm{eff}}$ end, the number of tracer star particles is only a few tens in the level-2 resolution, which is not enough to resolve the radial gradient. Additionally, we did not include 3σ clippings to the observed LOSVs in Figure 4, so the number of inflations can be much larger, as biased by some extreme velocities near the LOSV distribution tails.

Going back to Figure 7, in the bottom-right plot, we can see the velocity dispersions are not very well fit at large radii. The model is significantly higher than the actual dispersions along the major axis and beyond 30′. In the left panel, the model tends to fit a rotation of this dwarf system. This gives a good fit in central regions, but beyond 30′, the actual LOSVs do not show as strong a trend of rotation as those particles in the central regions. In fact, this dwarf system is undergoing some rotations in the central regions, but no such rotations in the outskirts. However, the model fails to capture such a feature, because we fix the rotation parameter, κ, to be the same for different MGE components (see Section 2.5 for details). As a result, the first and second moments are not very well fit in the outskirts. Allowing κ and b to differ for different MGE components can potentially improve the fitting, but our conclusions about how binary motions inflate or deflate the dynamical constraints are not affected.

We emphasize that f_{binary} adopted in model-Ib and Figure 5 is as high as 70%. This enables us to investigate a more significant trend, but in real observations, the binary fractions of MW satellite galaxies can vary significantly. We thus show in Figure 8 the result based on model-Ic, which has $f_{\mathrm{binary}} = 36\%$. The main trends remain very similar between Figure 5 and 8, in the sense that $M(< r_{\mathrm{half}})$ are all inflated after including binary motions, whereas M(200–300 pc) tend to be mostly deflated. The number of inflations in $M(< r_{\mathrm{half}})$ also slightly increases with the decrease in $\sigma_{v_r,\mathrm{eff}}$, though not as prominently as in Figure 5. With decreased f_{binary}, the number of inflations becomes $\sim$10% at $\sigma_{v_r,\mathrm{eff}}$ of 3 km s^{-1}. The number of deflations, on the other hand, does not show significant decrease, perhaps because the deflations are related to the gradient/shape in the velocity dispersion profile, instead of the absolute number of inflations in the overall velocity dispersion.

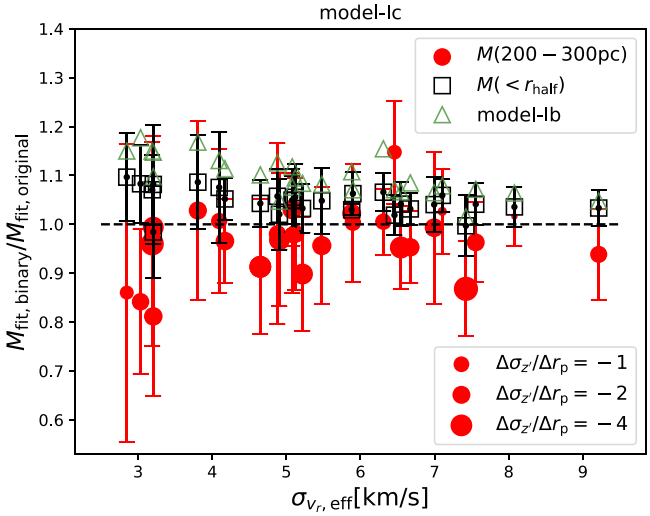

Figure 8. Similar to Figure 5, but based on an assumed binary fraction of 36% (model-Ic). Green triangles are repeats of the inflations in $M(< r_{\mathrm{half}})$ from model-Ib with a binary fraction of 70%, i.e., exactly the same as the black squares in Figure 5.

4.3. Model-II Applied to Scaled Level-3 Resolution

4.3.1. Error-free Case to Test the Model Dependence

With model-I, we have seen how binary motions affect the dynamical constraints in a radius-dependent way, because the velocity dispersions of realistic dwarf galaxies can show negative radial gradients. However, model-I (Duquennoy & Mayor 1991) is based on relatively old observations. In this subsection, we move on to consider model-II based on that of Moe & Di Stefano (2017), which considers joint distributions of different orbital elements and is based on more recent observations.

The results are shown in Figure 9 for $f_{\mathrm{binary}} = 70\%$ and 36%. Comparing to Figures 5 and 8 based on model-I, we can see the main trends remain very similar, when f_{binary} is the same but the binary orbital element distribution models are different. Despite the differences in the models, $M(< r_{\mathrm{half}})$ are almost all inflated, and M(200–300 pc) are more likely deflated. Red dots below unity on average have more negative radial gradients in their LOSV dispersion profiles. The green triangles are repeats of the black squares from Figures 5 and 8, which are consistent with the new measurements, indicating no prominent model dependencies.

4.3.2. Observational Errors and Multiepoch Data

Now we consider more realistic cases after including observational errors and the mock of two-epoch observations with model-II. Figure 10 is similar to the right plot of Figure 9. It is based on $f_{\mathrm{binary}} = 36\%$, but we have included a typical error of 3 km s^{-1} to the LOSVs. We can see the black squares and green triangles almost overlap with each other, despite the inclusion of observational errors. However, we also note in Figure 10 that the red dots are slightly more symmetrically distributed around unity than in the right plot of Figure 9, perhaps indicating the inclusion of observation errors can help us weaken the radial gradients in the LOSV dispersion profiles and the deflations in M(200–300 pc).

Note here that we only show the results after including observational errors for model-IIb-err, but not model-IIa-err.

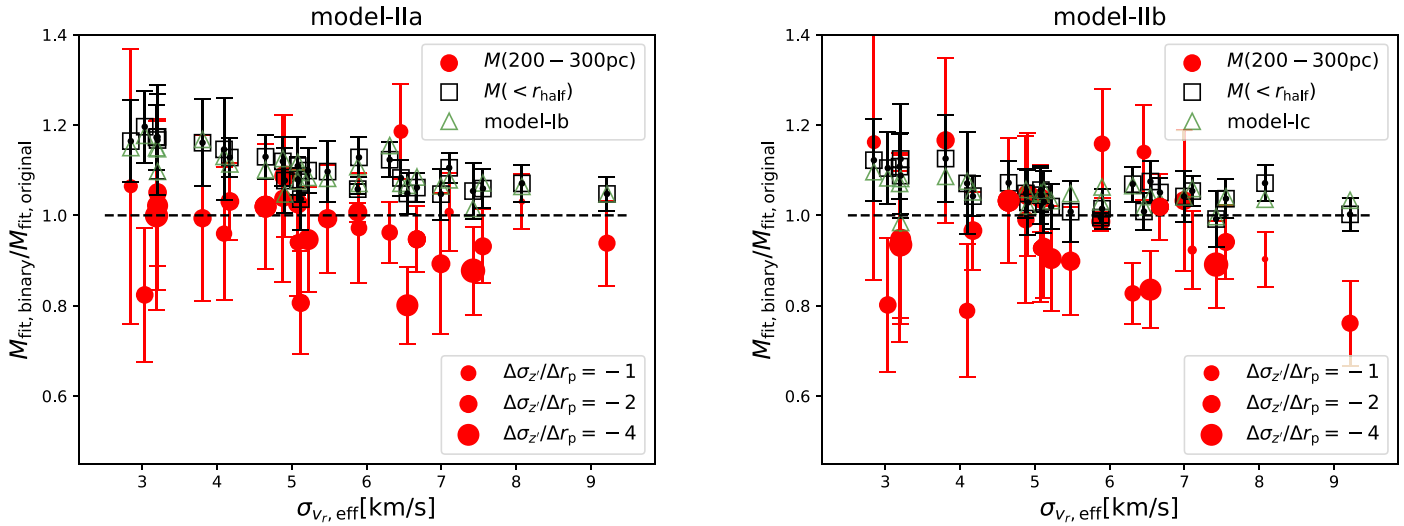

Figure 9. Left: similar to Figure 5, but based on model-IIa. The adopted binary fraction is 70%. Right: similar to Figure 8, but based on model-IIb. The adopted binary fraction is 36%. Green triangles in either plot show the inflations in $M(<r_{\mathrm{half}})$ from model-Ib (Figure 5) and model-Ic (Figure 8), with the same binary fractions with the corresponding black squares, but incorporating different binary orbital models. In both plots, the size of red dots is inversely proportional to the averaged radial gradient of the intrinsic LOSV dispersion profile over $0.2r_{\mathrm{half}}$ and $2r_{\mathrm{half}}$. The more negative the gradients are, the larger the symbol sizes.

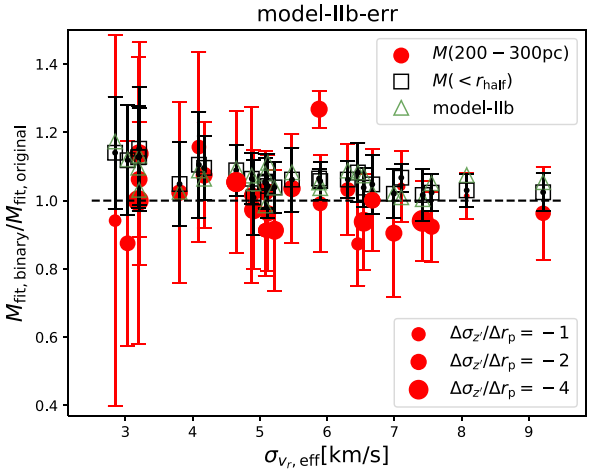

Figure 10. Similar to the right plot of Figure 9, but observational errors of 3 km s^{-1} have been added to the LOSVs (model-IIb-err with 36% of binary fraction). Note that model-IIa-err with a higher binary fraction of 70% shows very similar trends after including observational errors, so we choose not to repeatedly show the results.

This is because all trends based on the comparisons between model-IIa and model-IIa-err are very similar, i.e., we see very similar numbers of inflations in $M(<r_{\mathrm{half}})$, and the deflations in M(200–300 pc) are slightly weakened. So we avoid repeatedly showing the results.

For the results in Figure 11, we further exclude star particles which have more than 5 km s^{-1} of changes in their LOSVs over 1 yr. We create the LOSV for the second observation by adding 1 yr and recalculating the LOSV at the new true anomaly (f'). This 5 km s^{-1} of threshold is applied to the LOSVs after including binary motions and observational errors of 3 km s^{-1}. Once we determine the star particles to be excluded, they are excluded from the tracer populations both before and after including binary motions, though the threshold itself is determined after incorporating binaries.

In the left plot of Figure 11, 70% of the binary fraction still leads to ∼10% of inflations in $M(<r_{\mathrm{half}})$ at $\sigma_{v_r,\mathrm{eff}}\sim 3$ km s^{-1}, which drops to ∼1%–3% at 4–8 km s^{-1}. The deflations in M (200–300 pc) still exist, with more red dots below unity, but they become closer to unity, especially at $\sigma_{v_r,\mathrm{eff}}>5$ km s^{-1}. In the right plot, with the lower 36% of binary fraction, there is almost no systematic bias at every $\sigma_{v_r,\mathrm{eff}}$. The black squares stay very close to zero. The red dots in the right plot still have large scatters but no longer show prominent biases toward below unity. Our results thus indicate that with a nonextreme binary fraction, and typical observational errors of 3 km s^{-1} to the LOSVs, two epoch observations over 1 yr are enough to avoid binary orbital motions affecting the dynamical modeling outcomes at $3\ \mathrm{km\,s^{-1}}<\sigma_{v_r,\mathrm{eff}}<9\ \mathrm{km\,s^{-1}}$.

4.3.3. The 1–3 km s^{-1} Region

So far we have investigated how binaries affect the dynamical modeling outcomes at effective intrinsic velocity dispersions of $3\ \mathrm{km\,s^{-1}}<\sigma_{v_r,\mathrm{eff}}<9\ \mathrm{km\,s^{-1}}$. We have tried different binary orbital element distribution models, cases with or without observational errors, and mocks of multiepoch observations. Here we move on to investigate the region of $1\ \mathrm{km\,s^{-1}}<\sigma_{v_r,\mathrm{eff}}<3\ \mathrm{km\,s^{-1}}$. We scale up the binary orbital motions by a factor of 10.5, and apply JAM to dwarf galaxies with $\log_{10}M_*/M_\odot>7.5$ from AURIGA level-3 simulations. With the scaling of 10.5, we are equivalently investigating dwarfs with $1\ \mathrm{km\,s^{-1}}<\sigma_{v_r,\mathrm{eff}}<3\ \mathrm{km\,s^{-1}}$.

The results are shown in Figure 12. We have excluded tracer stars that have changes in their LOSVs greater than 5 km s^{-1} across two observations separated by 1 yr, subject to an observational error of 1 km s^{-1} in LOSVs. With $f_{\mathrm{binary}}=70\%$ and 36%, $M(<r_{\mathrm{half}})$ can still be significantly inflated by ∼60% and 30% at $\sigma_{v_r,\mathrm{eff}}\sim 1$ km s^{-1}. Over 1.5–3 km s^{-1}, the inflations in $M(<r_{\mathrm{half}})$ range from ∼28%–10% for a binary fraction of 70%. With a lower binary fraction of 36%, the number of inflations in $M(<r_{\mathrm{half}})$ is close to zero at 3 km s^{-1}, but reaches ∼15% to 5% at 1.5–2.5 km s^{-1}.

In comparison, M(200–300 pc) are not prominently deflated in the left plot of Figure 12. The red dots are distributed more symmetrically around the black horizontal dashed line in the left plot of Figure 12. Unlike previous figures, we do not see more red dots below unity. This is perhaps because with a high

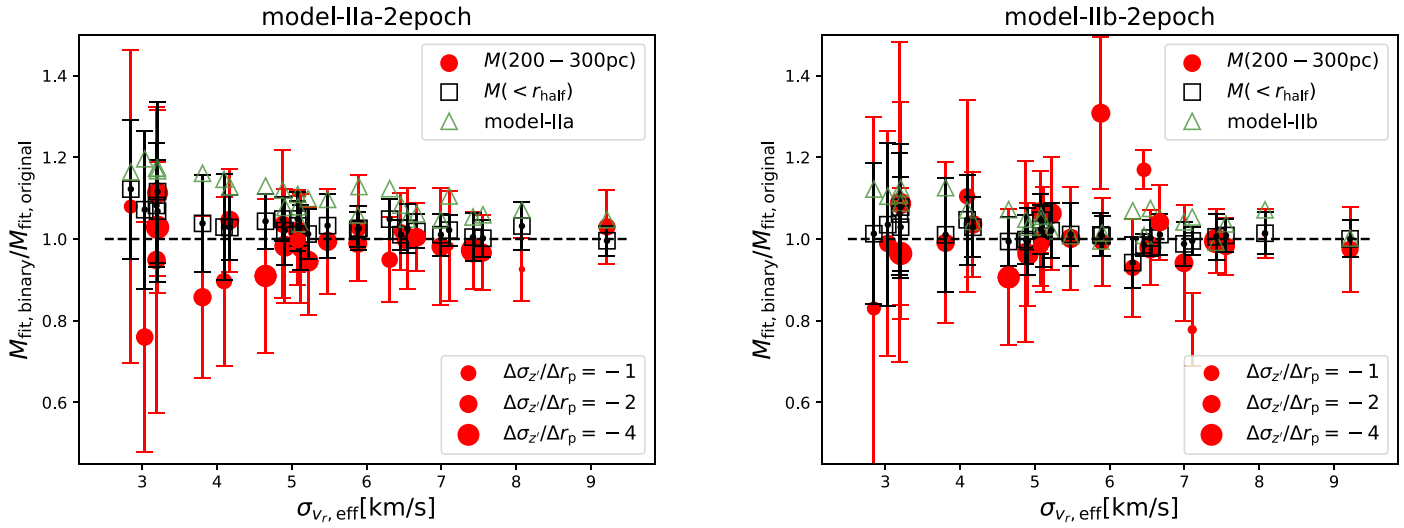

Figure 11. Left: similar to the left plot of Figure 9, but after including observational errors of 3 km s^{-1} in LOSVs and after incorporating binary orbital motions, we drop tracers whose changes in their LOSVs are greater than 5 km s^{-1} over 1 yr. This is based on model-IIa-2epoch with 70% of binary fraction. Right: similar to the left plot, but based on model-IIb-2epoch with 36% of binary fraction. In both plots, the size of red dots is inversely proportional to the averaged radial gradient of the LOSV dispersion profile over $0.2r_{\mathrm{half}}$ and $2r_{\mathrm{half}}$. The more negative the gradients are, the larger the symbol sizes.

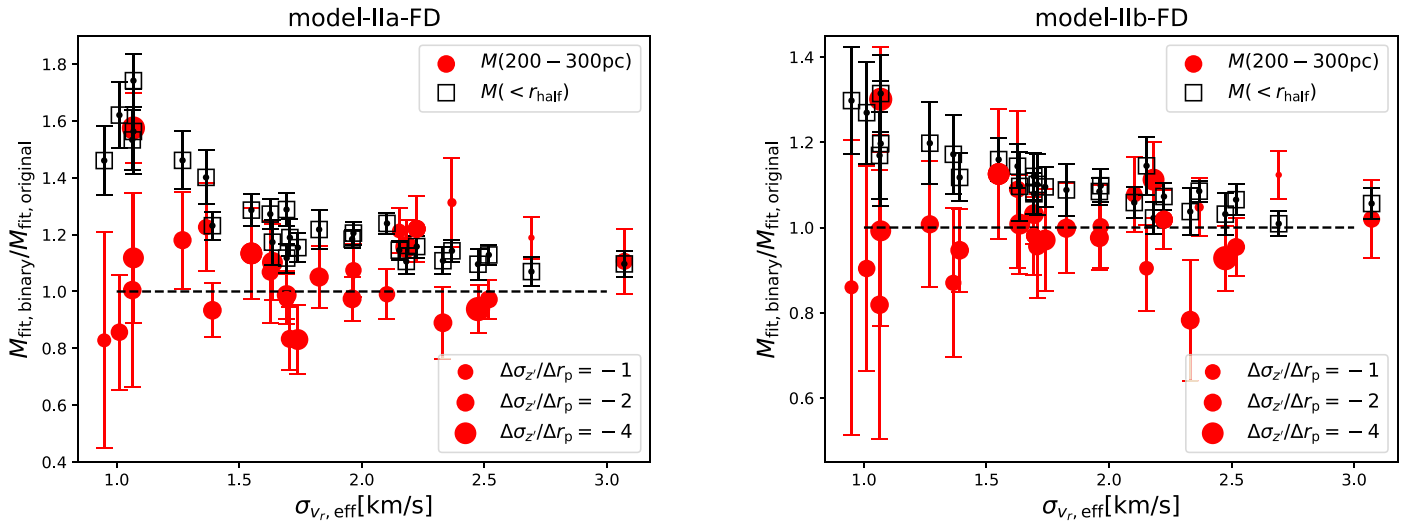

Figure 12. Similar to Figure 11, but based on model-IIa-FD ($f_{\mathrm{binary}}=70\%$) and model-IIb-FD ($f_{\mathrm{binary}}=36\%$) to investigate how binary motions affect the 1–3 km s^{-1} region in LOSV dispersions. The binary motions are scaled up by a factor of 10.5. Two epoch mock observations are adopted to exclude tracer stars with greater than 5 km s^{-1} of change in their LOSVs, after including observational error of 1 km s^{-1}. In both plots, the size of red dots is inversely proportional to the averaged radial gradients of the intrinsic LOSV dispersion profiles over $0.2r_{\mathrm{half}}$ and $2r_{\mathrm{half}}$. The more negative the gradients are, the larger the symbol sizes.

binary fraction of 70% and over the range of 1 km s^{-1} < $\sigma_{v_r,\mathrm{eff}}$ < 3 km s^{-1}, the fractional inflations in the velocity dispersions due to binary motions are very strong at every radius, and the radial gradients in the intrinsic velocity dispersions are no longer significant compared with the additional dispersions introduced by binary motions, and thus we do not see obvious deflations in M(200–300 pc). On the other hand and in the right plot of Figure 12, where f_{binary} gets lowered to 36%, we can still see the trend that there are more red dots below unity.

We thus conclude that for ultra-faint dwarf galaxies whose intrinsic velocity dispersions are close to 1 km s^{-1}, they are more significantly affected by the existence of binaries. This is true even for a mild binary fraction of 36% and after excluding tracer stars with prominent changes in the LOSVs with two epoch of observations.

In the end, we note that in real observations, the number of observed stellar tracers can be very small (from a few to a few tens only) for such ultra-faint dwarfs with 1 km s^{-1} < $\sigma_{v_r,\mathrm{eff}}$ < 3 km s^{-1}. In our analysis, we adopt a large sample of tracers, which do not fully represent the real case. Thus, our results in this subsection can only be regarded as an ensemble averaged behavior for a large sample of such ultra-faint dwarfs. In real observations, the dynamical constraints for dwarf galaxies with 1 km s^{-1} < $\sigma_{v_r,\mathrm{eff}}$ < 3 km s^{-1} can have large system-to-system scatters, and are expected to have large statistical errors depending on the tracer sample size.

5. Discussions and Conclusions

In this study, we investigate how binary orbital motions affect the dynamical modeling outcomes of dwarf galaxies, by using realistic tracers constructed from star particles for 17 and

28 dwarf galaxies from the AURIGA level-2 and level-3 suites of simulations.

Level-2 resolution only has one MW-like system, but it can have ∼40 star particles for dwarf galaxies with $M_* \sim 3 \times 10^4\,M_\odot$, which allows for direct and initial checks for the effect of binary motions. However, it still ends up with large statistical errors, and the internal dynamics of dwarf systems cannot be well resolved with a few tens of particles. Thus, we also select dwarf galaxies more massive than $10^{7.5}\,M_\odot$ from six MW-like systems of the level-3 resolution. We scale up the level of binary orbital motions by factors of 3.5 or 10.5, which is equivalent to decreasing the velocity dispersions of the dwarf galaxies. However, at the same time, we can have a sufficient number of tracer particles to ensure good statistics.

On the basis of the above mock dwarf systems and their tracer star samples, we incorporate binary orbital motions by sampling the orbital element distributions of binary systems based on observations of solar neighborhood stars (Duquennoy & Mayor 1991; Moe & Di Stefano 2017). We further apply the Jeans Anisotropic Multi-Gaussian expansion method (JAM) to investigate how the best-constrained dynamical mass is changed before and after incorporating the binaries.

For level-2 resolution and by sampling binary orbital motions from the Duquennoy & Mayor (1991) model with a 70% fraction of binaries, the number of inflations in the best-constrained dynamical mass prominently increases with the decrease in the LOSV dispersions (σ_{v_r}) of dwarf galaxies.

With level-3 resolution, we sample binary orbital motions from both the Duquennoy & Mayor (1991) model and the more recent Moe & Di Stefano (2017) model. The latter study has explicitly considered joint distributions of different orbital elements based on more recent observations. We find that the numbers of inflations/deflations and the overall trends with the above two orbital motion models are statistically consistent each other with the same binary fraction, indicating no prominent dependencies on binary orbital element distribution models.

Our major results are based on the Duquennoy & Mayor (1991) model, and we find the total masses within the half-mass radius of tracers, $M(<r_{\rm half})$, are all inflated after including binaries. They reach maximums of 15% for 70% of binary fraction ($f_{\rm binary}$) at an effective LOSV dispersion of $\sigma_{v_r,\rm eff} \sim 3\ {\rm km\ s^{-1}}$, which decreases to 10% for $f_{\rm binary} = 36\%$.

Interestingly, the dynamically constrained mass in central regions tend to be deflated after including binary motions. In particular, when the inflations in $M(<r_{\rm half})$ increase with the decrease in $\sigma_{v_r,\rm eff}$, the deflations in the central density do not show clear dependencies on $\sigma_{v_r,\rm eff}$. Dwarf galaxies with $\sigma_{v_r,\rm eff}$ in the range of 3–8 km s^{-1} can have their dynamically constrained central density deflated by up to 10%–20% due to binary motions. Additionally, such deflations do not show prominent dependences on $f_{\rm binary}$ either.

The deflations in the central density are due to the negative radial gradient in the velocity dispersion profiles. The velocity dispersion significantly decreases with increase in radius. As a result, the LOSV dispersions are much smaller in the outskirts, bringing in much more significant fractional increases at larger radius, and thus more significant inflations in the best-constrained dynamical masses in the outer regions. The fractional increase is much less significant in the central regions. Thus, the dynamical masses in the central regions are inflated less. In better fitting the velocity map in the outskirts, the best-constrained dynamical masses in inner regions are often deflated.

The deflation in the central density is important, because most previous studies based on Monte Carlo sampling of binary motions do not include radial gradients in their intrinsic velocity dispersions. Since binary motions inflate the intrinsic velocity dispersions, a general impression is held that the dynamically constrained masses of ultra-faint dwarf galaxies are inflated due to binary motions. We show in this study, for the first time, that the effect of binary motions on the dynamical mass constraints is radius dependent. In the inner regions, deflations are more likely to happen.

Moreover, since it is the total mass in the inner regions of dwarf galaxies that is more sensitive to the inner density slopes, the deflations in the central density can be more closely related to the core-cusp problem. Since binary orbital motions can deflate the inner dynamical mass, the inner density slopes can be underestimated. As a result, cuspy dwarf galaxies might be determined to be biased to cored if they have strong negative radial gradients in their velocity dispersion profiles. In fact, we have shown in Paper I that global contractions of the dwarf galaxies can result in underestimated inner density profiles for steady-state models. In particular, we have shown that for a few Sagittarius dwarf spheroid–like systems, the JAM constrained inner density profiles are significantly more flattened than in reality, on the basis of which the deflated central densities due to binaries can further make the best-constrained inner densities more flattened.

After including a 3 km s^{-1} observational error in the LOSVs, the trends remain very similar, but the deflations in the central density seem to be slightly weakened. By further discarding tracer star particles that have greater than 5 km s^{-1} changes in their LOSVs after including binary motions and 3 km s^{-1} of observational errors, we find the inflations decrease to almost zero for nonextreme binary fractions of 36%. Our results thus indicate that for nonextreme binary fractions of 30%–40%, and with typical observational errors to the LOSV and multiepoch data, binary orbital motions are unlikely to significantly affect the dynamical modeling outcome at $\sigma_{v_r,\rm eff} \sim$ 3–9 km s^{-1}. On the other hand, for more extreme binary fractions of 70%, there might still be $< \sim 10\%$ of inflations in $M(<r_{\rm half})$ at $\sigma_{v_r,\rm eff} \sim 3$ km s^{-1}, which is, however, not statistically significant compared with the errors in our analysis.

In the end, we investigate the region of 1 km s^{-1} $< \sigma_{v_r,\rm eff} <$ 3 km s^{-1}. We find even with two epoch observations spanning 1 yr to exclude stars whose changes in LOSVs are greater than 5 km s^{-1}, $M(<r_{\rm half})$ can still be significantly inflated by ∼60% and 30% at $\sigma_{v_r,\rm eff} \sim 1$ km s^{-1}, for binary fractions of 70% and 36%, respectively. At 1.4 km s^{-1} $< \sigma_{v_r,\rm eff} <$ 3 km s^{-1}, the inflations in $M(<r_{\rm half})$ range from ∼28% to 10% with binary fraction of 70%. With a binary fraction of 36%, the inflation in $M(<r_{\rm half})$ is close to zero at 3 km s^{-1}, but reaches ∼15% to 5% at 1.5–2.5 km s^{-1}.

Acknowledgments

This work was supported by NSFC (12022307, 12273021), the China Manned Space (CSST) project Nos. CMS-CSST-2021-A02 and CMS-CSST-2021-A08, the National Key Basic Research and Development Program of China (No. 2018YFA0404504), 111 project (No. B20019), and Shanghai Natural Science Foundation (No. 19ZR1466800). We thank the

sponsorship from Yangyang Development Fund. W.W. is grateful for discussions with Chao Liu and Haifeng Wang on binary orbital element distribution, with Kaiming Cui on calculation of stellar parameters, and with Haijun Tian on binary physics. We are appreciative for the invitation and hospitality from Sarah Bird and Haijun Tian during the 2022 Gaia Sprint event at the Three Gorges University. The computation of this work was carried out on the GRAVITY supercomputer at the Department of Astronomy, Shanghai Jiao Tong University, and is partly supported by the STFC DiRAC HPC Facility, at the Institute of Computational Cosmology (ICC), Durham University. L.Z. acknowledges funding from CAS Project for Young Scientists in Basic Research, grant No. YSBR-062, and National Natural Science Foundation of China under grant No. Y945271001. R.G. acknowledges financial support from the Spanish Ministry of Science and Innovation (MICINN) through the Spanish State Research Agency, under the Severo Ochoa Program 2020–2023 (CEX2019-000920-S), and support from an STFC Ernest Rutherford Fellowship (ST/W003643/1). Z.Z.L. acknowledges support by ISF grants 861/20, 3061/21, DFG/DIP, grant STE1869/2-1 GE625/17-1 and the MSCA Fellowship (101109759).

ORCID iDs

Wenting Wang https://orcid.org/0000-0002-5762-7571
Ling Zhu https://orcid.org/0000-0002-8005-0870
Yipeng Jing https://orcid.org/0000-0002-4534-3125
Robert J. J. Grand https://orcid.org/0000-0001-9667-1340
Zhaozhou Li https://orcid.org/0000-0001-7890-4964
Lu Li https://orcid.org/0000-0002-0880-3380
Jiaxin Han https://orcid.org/0000-0002-8010-6715
Ting S. Li https://orcid.org/0000-0002-9110-6163
Fabo Feng https://orcid.org/0000-0001-6039-0555
Carlos Frenk https://orcid.org/0000-0002-2338-716X

References

Amorisco, N. C., & Evans, N. W. 2012, ApJL, 756, L2
Battaglia, G., Helmi, A., Tolstoy, E., et al. 2008, ApJL, 681, L13
Bressan, A., Marigo, P., Girardi, L., et al. 2012, MNRAS, 427, 127
Bullock, J. S., & Boylan-Kolchin, M. 2017, ARA&A, 55, 343
Cappellari, M. 2008, MNRAS, 390, 71
Collins, M. L. M., Read, J. I., Ibata, R. A., et al. 2021, MNRAS, 505, 5686
Collins, M. L. M., Tollerud, E. J., Rich, R. M., et al. 2020, MNRAS, 491, 3496
de Blok, W. J. G. 2010, AdAst, 2010, 789293
de Blok, W. J. G., McGaugh, S. S., & Rubin, V. C. 2001, AJ, 122, 2396
Delsemme, A. H. 1987, A&A, 187, 913
Duquennoy, A., & Mayor, M. 1991, A&A, 248, 485
Eggleton, P. P. 1983, ApJ, 268, 368
El-Badry, K., Rix, H. W., & Heintz, T. M. 2021, MNRAS, 506, 2269
Faucher-Giguère, C. A., Lidz, A., Zaldarriaga, M., & Hernquist, L. 2009, ApJ, 703, 1416
Feast, M. W., Thackeray, A. D., & Wesselink, A. J. 1961, MNRAS, 122, 433
Feng, F., & Bailer-Jones, C. A. L. 2014, MNRAS, 442, 3653
Flores, R. A., & Primack, J. R. 1994, ApJL, 427, L1
Gaia Collaboration, Arenou, F., Babusiaux, C., et al. 2023, A&A, 674, A34
Genina, A., Benítez-Llambay, A., Frenk, C. S., et al. 2018, MNRAS, 474, 1398
Gentile, G., Salucci, P., Klein, U., Vergani, D., & Kalberla, P. 2004, MNRAS, 351, 903
Grand, R. J. J., Gómez, F. A., Marinacci, F., et al. 2017, MNRAS, 467, 179
Grand, R. J. J., Helly, J., Fattahi, A., et al. 2018, MNRAS, 481, 1726
Grand, R. J. J., Marinacci, F., Pakmor, R., et al. 2021, MNRAS, 507, 4953
Gunn, J. E., & Gott, J. R. I. 1972, ApJ, 176, 1
Hargreaves, J. C., Gilmore, G., & Annan, J. D. 1996, MNRAS, 279, 108
Higuchi, A. 2020, AJ, 160, 134
Koposov, S. E., Gilmore, G., Walker, M. G., et al. 2011, ApJ, 736, 146
Kroupa, P. 2002, Sci, 295, 82
Liu, C. 2019, MNRAS, 490, 550
Martin, N. F., Ibata, R. A., Chapman, S. C., Irwin, M., & Lewis, G. F. 2007, MNRAS, 380, 281
Martin, N. F., McConnachie, A. W., Irwin, M., et al. 2009, ApJ, 705, 758
McConnachie, A. W., & Côté, P. 2010, ApJL, 722, L209
McConnachie, A. W., Huxor, A., Martin, N. F., et al. 2008, ApJ, 688, 1009
Minor, Q. E. 2013, ApJ, 779, 116
Minor, Q. E., Martinez, G., Bullock, J., Kaplinghat, M., & Trainor, R. 2010, ApJ, 721, 1142
Minor, Q. E., Pace, A. B., Marshall, J. L., & Strigari, L. E. 2019, MNRAS, 487, 2961
Moe, M., & Di Stefano, R. 2017, ApJS, 230, 15
Moore, B. 1994, Natur, 370, 629
Murray, C. D., & Correia, A. C. M. 2010, in Exoplanets, ed. S. Seager (Tucson, AZ: Univ. Arizona Press), 15
Okamoto, T., Frenk, C. S., Jenkins, A., & Theuns, T. 2010, MNRAS, 406, 208
Orkney, M. D. A., Read, J. I., Rey, M. P., et al. 2021, MNRAS, 504, 3509
Pace, A. B., Kaplinghat, M., Kirby, E., et al. 2020, MNRAS, 495, 3022
Pakmor, R., & Springel, V. 2013, MNRAS, 432, 176
Pakmor, R., Gómez, F. A., Grand, R. J. J., et al. 2017, MNRAS, 469, 3185
Pianta, C., Capuzzo-Dolcetta, R., & Carraro, G. 2022, ApJ, 939, 3
Pillepich, A., Nelson, D., Springel, V., et al. 2019, MNRAS, 490, 3196
Planck Collaboration, Ade, P. A. R., & Aghanim, N. 2014, A&A, 571, A16
Raghavan, D., McAlister, H. A., Henry, T. J., et al. 2010, ApJS, 190, 1
Schaye, J., Crain, R. A., Bower, R. G., et al. 2015, MNRAS, 446, 521
Simon, J. D. 2019, ARA&A, 57, 375
Simon, J. D., & Geha, M. 2007, ApJ, 670, 313
Spencer, M. E., Mateo, M., Olszewski, E. W., et al. 2018, AJ, 156, 257
Spencer, M. E., Mateo, M., Walker, M. G., et al. 2017, AJ, 153, 254
Springel, V. 2010, MNRAS, 401, 791
Springel, V., Di Matteo, T., & Hernquist, L. 2005, MNRAS, 361, 776
Springel, V., & Hernquist, L. 2003, MNRAS, 339, 289
Tian, H. J., El-Badry, K., Rix, H. W., & Gould, A. 2020, ApJS, 246, 4
Torrealba, G., Koposov, S. E., Belokurov, V., & Irwin, M. 2016, MNRAS, 459, 2370
Torrealba, G., Belokurov, V., Koposov, S. E., et al. 2019, MNRAS, 488, 2743
Vogelsberger, M., Genel, S., Sijacki, D., et al. 2013, MNRAS, 436, 3031
Wang, W., Han, J., Cautun, M., Li, Z., & Ishigaki, M. N. 2020, SCPMA, 63, 109801
Wang, W., Han, J., Cooper, A. P., et al. 2015, MNRAS, 453, 377
Wang, W., Zhu, L., Li, Z., et al. 2022, ApJ, 941, 108
Watkins, L. L., van de Ven, G., den Brok, M., & van den Bosch, R. C. E. 2013, MNRAS, 436, 2598
Zhu, L., van de Ven, G., Watkins, L. L., Posti, L., et al. 2016a, MNRAS, 463, 1117
Zhu, L., Romanowsky, A. J., van de Ven, G., et al. 2016b, MNRAS, 462, 4001